Cell morphogenesis via shape-guided self-propelled treadmilling actin waves

Kio Yagami[1], Kentarou Baba[1], Shinji Misu[1], Hiroko Katsuno-Kambe[1], Takunori Minegishi[1], Kazunori Okano[2], Yuichi Sakumura[3], Yoichiroh Hosokawa[2] and Naoyuki Inagaki[1,*]

[1]Laboratory of Systems Neurobiology and Medicine, Division of Biological Science, Nara Institute of Science and Technology, Ikoma, Nara 630-0192, Japan.

[2]Bio-Process Engineering Laboratory, Division of Materials Science, Nara Institute of Science and Technology, Ikoma, Nara 630-0192, Japan.

[3]Laboratory of Data-driven Biology, Division of Biological Science, Nara Institute of Science and Technology, Ikoma, Nara 630-0192, Japan.

*e-mail: ninagaki@bs.naist.jp

Abstract

Actin dynamics mediate cell morphogenesis and motility. Actin filaments polymerise outward at cell protrusions such as the leading edge of migrating cells, thereby pushing the membrane to protrude. The current paradigm explains that actin dynamics are biochemically regulated by signalling pathways. However, it remains unclear whether these signal-driven mechanisms alone are sufficient to regulate local actin polymerisation at cell protrusions. Here, we show that cell shape can also regulate actin dynamics. We found that arrays of actin filaments emerge widely in glioma cells and translocate as actin waves in the direction of polymerisation through treadmilling, i.e. directional polymerisation and disassembly. The arrival of actin waves at the cell periphery pushes the plasma membrane to form protrusions (filopodia and lamellipodia). Furthermore, actin waves accumulate at protrusions even in the absence of local signalling cues, similar to self-propelled particles (active particles) colliding with a boundary, thereby leading to further expansion of protrusions for cell polarisation and migration. The shape-guided actin accumulation constitutes a positive feedback interaction with actin-mediated cell protrusion and mediates an effective lateral inhibition, thereby conferring robustness to the classical pathway of cellular morphogenesis. Because actin filaments undergo treadmilling in various protrusions, we propose that the cell shape-guided and self-propelled movement is a basic property of treadmilling actin filaments that mediates robust cell morphogenesis and motility.

Introduction

Spatial regulation of actin dynamics is crucial for controlling force, cell shape and motility[1-4]. Dynamic actin filaments are located in various cell protrusions, where they polymerise outward and push the membrane to protrude. In many cases, they disassemble proximally, which results in treadmilling of the filament arrays[1-5]. During this process, ATP-bound actin monomers assemble at the plus ends of actin filaments and ATP is hydrolysed within the filaments. The filaments disassemble from the minus end because they are destabilised by ADP-bound actin molecules. ADP in the subunit is replaced with ATP, which allows the subunit to be reused for polymerisation. Thus, actin filaments undergo directional polymerisation and disassembly using the energy derived from ATP hydrolysis[1-5]. The prevailing view is that actin filament nucleators and elongators, such as the Arp2/3 complex, formins, FMNL and Ena/VASP, control local actin assembly under Rho GTPase signalling[1,3,4]. On the other hand, actin disassembly-promoting proteins, such as ADF/cofilin, regulate actin turnover[2,5,6]. However, it remains unclear whether these signal-driven mechanisms alone are sufficient to regulate local actin dynamics at cell protrusions.

Accumulating evidence indicates that dynamic actin filaments undergo wave-like propagations in various cell types[7-10]. Many of these propagations have been explained by the reaction-diffusion mechanism[8-11]. On the other hand, we previously reported that actin treadmilling propels the translocation of actin waves and actin-binding proteins towards neurite tips[12]. In this study, we identified actin waves that translocate via treadmilling instead of the reaction-diffusion mechanism in non-neuronal cells. The arrival of actin waves at the cell periphery results in the formation of protrusions. Moreover, the actin waves spontaneously accumulated at cell protrusions even without local signalling in a manner similar to self-propelled particles (active particles), as described in the current literature on physics[13-15] and materials science[16]. This shape-guided and self-propelled movement mediates the accumulation of outward-polymerising actin filaments in protruding regions.

Results

Actin waves emerge widely in cells

To investigate the mechanism underlying the spatial regulation of actin dynamics, we

67 analysed a subline of glioma U251 cells that actively form lamellipodia (arrows,
68 Extended Data Fig. 1a) and filopodia (arrowheads). These cells spontaneously polarise
69 and migrate in the absence of growth factor stimulation (Extended Data Fig. 1b)[17]. Actin
70 dynamics were visualised by total internal reflection fluorescence (TIRF) microscopy
71 using the actin filament marker LifeAct (Fig. 1a and Supplementary Video 1). In
72 addition to prominent actin filaments at the leading edge (asterisk, Fig. 1a), arrays of
73 actin filaments that form filopodium-like structures (arrowheads, Fig. 1b) and
74 lamellipodium-like structures (arrows, Fig. 1c) emerged widely in the cytoplasm,
75 moved in random directions, and disappeared (Supplementary Video 1). Some
76 filopodium-like structures extended from the lamellipodium-like structures (yellow
77 arrowheads, Extended Data Fig. 1c, Supplementary Video 2), whereas
78 lamellipodium-like structures expanded from the filopodium-like structures (blue
79 arrow), indicating their interchangeability. Similar actin waves were also observed in
80 COS7 cells (Extended Data Fig. 1d, Supplementary Video 3), suggesting that they are
81 not cell type-specific. Herein, we analysed the filopodium-like and lamellipodium-like
82 structures that move within the cells as filopodium-type and lamellipodium-type actin
83 waves, respectively.
84 A combination of TIRF microscopy, which visualises the region near the
85 ventral plasma membrane, and epifluorescence microscopy, which visualises the entire
86 cell thickness, revealed a large fraction of waves translocating along the ventral plasma
87 membrane (arrowheads, Extended Data Fig. 1e, Supplementary Video 4), as well as
88 waves travelling apart from the adhesive substrate (arrowheads, Extended Data Fig. 1f,
89 Supplementary Video 4). In addition, 3D imaging with confocal deconvolution
90 microscopy revealed actin waves moving along the dorsal plasma membrane (Fig. 1d)
91 as well as waves translocating through the cytoplasm without interacting with the
92 plasma membrane (Fig. 1e, Supplementary Video 5).
93
94 **Actin waves translocate by treadmilling**
95 Next, we examined the actin dynamics within waves by labelling actin filaments with
96 EGFP-LifeAct, and monitoring actin molecules in waves by speckle imaging of
97 HaloTag-actin[18]. During the forward translocation of filopodium-type and
98 lamellipodium-type actin waves along the ventral membrane (green lines, Fig. 1f and

Extended Data Fig. 2a) individual actin molecules moved retrogradely within the filaments (magenta lines, Supplementary Video 6). Similar retrograde movements of actin molecules were observed in filopodium-type waves with no interaction with the plasma membrane (Extended Data Fig. 2b), indicating that actin waves undergo treadmilling and translocate in the direction of polymerisation.

We previously reported actin waves that translocate along neuronal nascent axons through treadmilling[9,12]: their front and rear ends undergo polymerisation and disassembly, respectively (black arrows, Fig. 1g, left)[9,12]. In addition, actin filaments in waves are weakly anchored to the plasma membrane and adhesive substrate, through the clutch-linker molecules shootin1a and cortactin as well as the cell adhesion molecule L1[12,19] (Fig. 1g, left). This anchoring impedes the retrograde flow (slippage) of treadmilling actin filaments (magenta arrow, Fig. 1g); thus, the actin polymerisation/disassembly rate exceeds the retrograde flow rate, which results in the forward translocation of the front and rear ends of waves (green arrow). During the translocation, the local concentrations of actin subunits and actin-binding proteins decrease at the front by polymerisation and increase at the rear by disassembly, resulting in their directional diffusion along the local concentration gradients (black arrows, Fig. 1g). Thus, accompanied by the directional diffusion, treadmilling actin waves mediate the translocation of actin and actin-binding proteins along axons[12,20].

Immunoblot analyses revealed that U251 cells express, shootin1b, cortactin and L1 (Extended Data Fig. 2c); shootin1b is a splicing variant of shootin1a that also mediates the actin-L1 linkage[21]. Shootin1b co-localised with actin filaments in lamellipodia (Extended Data Fig. 2d) and waves (arrowheads, Extended Data Fig. 2e). Inhibition of actin polymerisation in waves by cytochalasin B at a low concentration (0.05 μM)[12] decreased the velocity of actin wave translocation (Extended Data Fig. 2f). The Arp2/3 complex inhibitor CK666 (100 μM)[22] or a relatively non-specific formin inhibitor SMIFH2 (5 μM)[23] also reduced the velocity of actin wave (Fig. 1h), indicating that wave translocation is propelled by actin assembly. Furthermore, shootin1b knockout (KO) resulted in an increased retrograde flow rate of actin filaments in waves without affecting the polymerisation rate (Fig. 1i and Extended Data Fig. 2g), indicating that shootin1b anchors treadmilling actin filaments to the plasma membrane and adhesive substrate (Extended Data Fig. 2h). This in turn reduced the velocity of actin

wave translocation (Fig. 1i). Taken together, these results indicate that actin waves in U251 cells translocate via their treadmilling and that shootin1b promotes their translocation by impeding the retrograde flow (Fig. 1g, left)[12]. Actin waves may also move via treadmilling, without anchoring to the membrane (Fig. 1e), when actin filament retrograde flow is mechanically impeded in a viscous intracellular environment (Fig. 1g, right; see supplementary discussion).

Actin waves as precursors of protrusions

Interestingly, we observed filopodium-type waves entering into pre-existing lamellipodia and filopodia (arrowheads, Fig. 2a and b, Supplementary Video 7). The wave entry resulted in local actin filament accumulation and lamellipodial expansion (Fig. 2a, Supplementary Video 7). In addition, when lamellipodium-type and filopodium-type waves arrived at the plasma membrane, which does not form a protrusion, they pushed the membrane, resulting in the formation of lamellipodia as reported[24,25] (yellow arrows, Fig. 2c, Supplementary Video 8) and filopodia (arrowheads, Fig. 2d, Supplementary Video 9), respectively. Some filopodia and lamellipodia continued to move laterally along the membrane (Fig. 2c, d), consistent with previous reports that filopodia and lamellipodia move dynamically along the lateral side of neuronal[20,26] and non-neuronal[27,28] cells. We also noted lamellipodium-type waves that merged with the pre-existing lamellipodia through their lateral movement (yellow arrows, Fig. 2c, Supplementary Video 8).

If the lateral movements of filopodia and lamellipodia are driven by the mechanism of wave translocation, their velocity may be related to the angle θ of the polymerising actin filaments with respect to the membrane (Fig. 2e). To examine this possibility, we focused on the motion of filopodium-type waves because filopodium-type and lamellipodium-type waves are interchangeable (Extended Data Fig. 1c) and it was difficult to monitor the direction of actin filaments in lamellipodium-type waves (Fig. 1c). Time-lapse measurements of both the angle θ and the velocity of the filopodial lateral movement (V_L) (Fig. 2f, Supplementary Video 10) demonstrated that the velocity closely matched the cosine θ for the average velocity of the ventrally translocating filopodium-type waves before arriving at the membrane (V_V) (2.0 ± 0.2 μm/min, Figs. 1i, 2f), indicating agreement between the data and the prediction based

on the mechanism. Together, these findings suggest that treadmilling actin waves and filopodia/lamellipodia are equivalent structures and that actin waves serve as precursors of filopodia and lamellipodia. Therefore, the filopodia and lamellipodia that move laterally along the membrane are also termed actin waves in the present study.

Actin waves accumulate at protrusions

Intriguingly, we observed the accumulation of filopodium-type and lamellipodium-type actin waves in protrusive regions owing to their lateral movement (Fig. 3a, b, Supplementary Video 11), suggesting that actin dynamics are influenced by cell shape. In addition, a previous study reported that different cell types confined to square adhesive islands preferentially extend filopodia and lamellipodia from their corners[27]. To determine the potential influence of cell shape on actin dynamics, we prepared a triangular pattern of adhesive laminin on the substrate (Extended Data Fig. 3a). U251 cells showed the triangular shape when cultured on the laminin-coated adhesive island (Fig. 3c). While actin filaments were preferentially localised at the leading edge of unconstrained cells (Extended Data Fig. 1a), they accumulated at the corners of triangular cells (Fig. 3c). Live imaging of U251 cells labelled with LifeAct-mCherry revealed the dynamic accumulation of actin filaments at the corners (Fig. 3d and Supplementary Video 12). Actin waves travelled along the lateral edge, resulting in local accumulation of actin filaments at the corners upon arrival (arrowheads). Notably, in contrast to the current paradigm that the Arp2/3 complex promotes membrane protrusion by activating actin polymerisation, a component of the Arp2/3 complex, ARPC2, accumulated together with actin filaments at the protruding corners in the absence of local signalling (Fig. 3c).

Since the arrival of actin waves increased actin filaments at the protrusive areas (arrowheads, Fig. 3d), we hypothesised that actin waves mediate the accumulation of actin filaments at cell protrusions. To examine this possibility, we constructed a mathematical model to describe filopodium-type waves because actin filaments were clearly observed in these waves (Fig. 1b). Our model consists of the following properties of actin wave dynamics (see Methods).

1. Actin waves emerge at random locations within the cell and move in random

directions.

2. Actin waves frequently change their direction of translocation and disappear at the end of their lifetime.
3. Actin waves re-emerge at the location where the preceding waves disappear.
4. Actin waves located at the cell periphery move laterally along the cell membrane. The direction and velocity of the lateral movement conform to the cosθ of the mean velocity of ventrally translocating waves (V_V), where θ is the angle of the direction of actin filaments relative to the cell membrane (Fig. 2f).

All the model parameters, i.e., lifetime, length, moving velocity and degree of the change in moving direction, were obtained from our quantitative experimental data (Extended Data Fig. 4, Extended Data Table 1). The actin waves described by the model accumulated at the corners of the triangular cells (Fig. 3e and Supplementary Video 13), as observed in U251 cells (Fig. 3c). Using this mathematical model, we further analysed the movement of the actin wave in cells with different corner angles (i.e. 30°, 60°, 120° or 180°; Extended Data Fig. 3b) and quantified the relative accumulation of actin filaments at the cell periphery and corners (Extended Data Fig. 3c). The actin waves accumulated at the cell periphery (Extended Data Fig. 3d). Furthermore, the accumulation of actin waves increased as the corner angle decreased from 180° to 30° (Fig. 3f). To validate this model, we cultured U251 cells using the same patterns. As predicted, actin filaments accumulated at the periphery (Extended Data Fig. 3e) and corners of the cells in a corner angle-dependent manner (Fig. 3g).

We further examined the effect of inhibiting the actin wave via knocking out shootin1b. Interestingly, shootin1b KO not only reduced the translocation velocity (Fig. 1i) but also the lifetime (Extended Data Fig. 4a-c) of actin waves. Introduction of these parameters (i.e. wave velocity and lifetime derived from shootin1b KO cells) into the model disrupted actin accumulation at the cell periphery and corners (Fig. 3h and Supplementary Video 13). Consistently, shootin1b KO inhibited actin accumulation at the cell periphery and corners of U251 cells (Fig. 3i). Taken together, the findings indicate that treadmilling actin waves mediate actin filament accumulation at the cell periphery and protrusions.

Actin waves mediate cell morphogenesis

As shown above, the inhibition of actin wave movement by shootin1b KO disrupted the accumulation of actin filamentsat the periphery and corners of shape-constrained cells (Fig. 3h-i) without affecting the actin polymerisation (Fig. 1i). Finally, the role of the actin wave in cell morphogenesis was analysed using cells with a deformable plasma membrane. Shootin1b KO resulted in the fragmentation of lamellipodia (Fig. 4a), thereby decreasing the lamellipodial coverage rate at the cell periphery (Fig. 4b and Extended Data Fig. 5a) and reducing filopodial length (Extended Data Fig. 5b). Furthermore, shootin1b depletion disrupted the unilateral integration of lamellipodium, resulting in a decrease in the degree of cell polarity (Fig. 4c). To further analyse how actin waves drive cell polarisation, we monitored the recovery of cell morphology following latrunculin A-induced actin filament disassembly[29]. Treatment of wild-type (WT) U251 cells with 100 nM latrunculin A disrupted their polarised morphology (Fig. 4d and Supplementary Video 14). During recovery following latrunculin A washout, the cells formed multiple foci of small lamellipodia enriched with actin filaments (asterisks, Fig. 4d). The foci then grew (yellow arrows) and expanded laterally (blue arrows), eventually integrating into a large lamellipodia. In contrast, shootin1b deletion inhibited the expansion and integration of lamellipodium foci (asterisks, Fig. 4e), thereby delaying the onset of cell migration after recovery from the latrunculin A treatment (Fig. 4f).

These finding suggest that cell shape-guided movement of treadmilling actin waves boosts actin-dependent cell morphogenesis and motility. In glioma cells, actin waves arrived at the plasma membrane (green arrows, Extended Data Fig. 6) aligned randomly oriented actin filaments to outward polymerisation and pushed the membrane to protrude (white arrows). They accumulated spontaneously at cell protrusions (red arrows), resulting in their further enlargement. Through lateral expansion (yellow arrow), the protrusions were integrated into a large leading edge of the front. These processes would cooperate with other mechanisms, including myosin II-mediated contraction at the rear[17,30] to polarise cells and drive cell migration.

Discussion

Treadmilling is an inherent property of actin dynamics. We demonstrated that arrays of

treadmilling actin filaments emerge widely in glioma cells and move as actin waves in the direction of polymerisation. Contrary to the classical pathway, in which actin nucleators promote cell protrusion by activating actin polymerisation (black arrows, Fig. 5a), actin filaments and the Arp2/3 complex component ARPC2 accumulated in cell protrusions in the absence of local signalling (Fig. 3a-c). Their corner angle-dependent accumulation (Fig. 3e-g) is similar to the motion of self-propelled particles, which are described in the fields of current physics[13,15] and soft matter[16]. Although we do not rule out actin waves that travel via other mechanisms, this analogy supports our conclusion that the treadmilling actin waves move as self-propelled machinery rather than via the reaction-diffusion mechanism. Treadmilling actin waves are not stable particles, but they continuously exchange actin subunits between the cytoplasm during translocation (Fig. 1g)[12].

The shape-guided self-propelled movement of actin waves provides a new framework for understanding the mechanism of cell morphogenesis (Fig. 5). First, the shape-guided actin accumulation (green arrow, Fig. 5a) constitutes a positive feedback interaction with actin-mediated cell protrusion (red box), thereby conferring robustness to the classical pathway of cellular morphogenesis (black arrows) under the regulation of signalling (blue arrow). Second, in the longstanding model of morphogenesis, i.e. local-excitation-global-inhibition (LEGI) model[30,31], a local activator of protrusion generates a global inhibitor (e.g. a molecule or membrane tension) that propagates laterally to suppress lateral protrusion (blue, dotted lines, Fig. 5b). However, the inhibitor would decay during the lateral propagation either by molecular diffusion or by membrane stretching (blue line, Fig. 5b). Furthermore, it would also inhibit the activated area, hampering the specific inhibition in the lateral regions (blue line). On the other hand, the self-propelled model does not require a global inhibitor because the translocation of the activator (actin wave) to the protrusion results in its lateral decrease, thereby suppressing protrusive activities laterally (blue arrows, Fig. 5c). Thus, this model offers a simple framework of effective lateral inhibition for cell morphogenesis (blue line). Finally, the present cell shape-sensitive system can respond not only to signalling but also to extracellular topographic cues that deform the plasma membrane from outside (yellow arrow, Fig. 5a) (Fig. 3e-g). This would enable cells to navigate

flexibly in three-dimensional environments through mechanical barriers and tissue pores[11,32-34].

Notably, recent simulation and microswimmer studies have reported that self-propelled particles in vesicles induce various shape deformations and movements similar to those observed in living cells[16,35-37]. Different actin-binding proteins and physical interactions could control the mode of protrusion, either extension or expansion, by altering the shape of the treadmilling filament arrays[3,4,38]. Because actin filaments undergo treadmilling in various protrusions (e.g., lamellipodia and filopodia of migrating cells[1,3,4], neurite tips and dendritic spines of neurons[39-42], microvilli and cell-cell adhesion sites of epithelial cells[43-46], hair cell stereocilia[47], invadopodia[48,49], and phagocytosis cups[50]), treadmilling actin waves may mediate various processes of cell morphogenesis and motility.

References

1 Pollard, T. D. & Borisy, G. G. Cellular motility driven by assembly and disassembly of actin filaments. *Cell* **112**, 453-465 (2003).

2 Bernstein, B. W. & Bamburg, J. R. ADF/cofilin: a functional node in cell biology. *Trends Cell Biol.* **20**, 187-195 (2010).

3 Carlier, M. F. & Shekhar, S. Global treadmilling coordinates actin turnover and controls the size of actin networks. *Nat. Rev. Mol. Cell Biol.* **18**, 389-401, doi:10.1038/nrm.2016.172 (2017).

4 Rottner, K. & Schaks, M. Assembling actin filaments for protrusion. *Curr. Opin. Cell Biol.* **56**, 53-63 (2019).

5 Goode, B. L., Eskin, J. & Shekhar, S. Mechanisms of actin disassembly and turnover. *J. Cell Biol.* **222** (2023).

6 Vitriol, E. A., Wise, A. L., Berginski, M. E., Bamburg, J. R. & Zheng, J. Q. Instantaneous inactivation of cofilin reveals its function of F-actin disassembly in lamellipodia. *Mol. Biol. Cell* **24**, 2238-2247 (2013).

7 Carlsson, A. E. Actin dynamics: from nanoscale to microscale. *Annu. Rev. Biophys.* **39**, 91-110 (2010).

8 Allard, J. & Mogilner, A. Traveling waves in actin dynamics and cell motility. *Curr. Opin. Cell Biol.* **25**, 107-115 (2013).

9 Inagaki, N. & Katsuno, H. Actin waves: origin of cell polarization and migration? *Trends Cell Biol.* **27**, 515-526 (2017).

10 Beta, C., Edelstein-Keshet, L., Gov, N. & Yochelis, A. From actin waves to mechanism and back: How theory aids biological understanding. *eLife* **12** (2023).

11 Weiner, O. D., Marganski, W. A., Wu, L. F., Altschuler, S. J. & Kirschner, M. W. An actin-based wave generator organizes cell motility. *PLoS Biol.* **5**, e221 (2007).

12 Katsuno, H. *et al.* Actin migration driven by directional assembly and disassembly of membrane-anchored actin filaments. *Cell Rep.* **12**, 648-660 (2015).

13 Kaiser, A., Wensink, H. H. & Lowen, H. How to capture active particles. *Phys. Rev. Lett.* **108**, 268307 (2012).

14 Elgeti, J., Winkler, R. G. & Gompper, G. Physics of microswimmers--single particle motion and collective behavior: a review. *Rep. Prog. Phys.* **78**, 056601 (2015).

15 Bechinger, C. *et al.* Active particles in complex and crowded environments. *Rev. Mod. Phys.* **88**, 045006 (2016).

16 Vutukuri, H. R. *et al.* Active particles induce large shape deformations in giant lipid vesicles. *Nature* **586**, 52-56 (2020).

17 Vassilev, V., Platek, A., Hiver, S., Enomoto, H. & Takeichi, M. Catenins steer

342 cell migration via stabilization of front-rear polarity. *Dev. Cell* **43**, 463-479
343 (2017).
344 18 Minegishi, T., Fujikawa, R., Kastian, R. F., Sakumura, Y. & Inagaki, N. Analyses
345 of actin dynamics, clutch coupling and traction force for growth cone advance. *J.*
346 *Vis. Exp.*, e63227 (2021).
347 19 Kubo, Y. *et al.* Shootin1-cortactin interaction mediates signal-force transduction
348 for axon outgrowth. *J. Cell Biol.* **210**, 663-676, doi:10.1083/jcb.201505011
349 (2015).
350 20 Flynn, K. C., Pak, C. W., Shaw, A. E., Bradke, F. & Bamburg, J. R. Growth
351 cone-like waves transport actin and promote axonogenesis and neurite branching.
352 *Dev. Neurobiol.* **69**, 761-779 (2009).
353 21 Minegishi, T. *et al.* Shootin1b mediates a mechanical clutch to produce force for
354 neuronal migration. *Cell Rep.* **25**, 624-639.e626 (2018).
355 22 Nolen, B. J. *et al.* Characterization of two classes of small molecule inhibitors of
356 Arp2/3 complex. *Nature* **460**, 1031-1034 (2009).
357 23 Nishimura, Y. *et al.* The formin inhibitor SMIFH2 inhibits members of the
358 myosin superfamily. *J. Cell Sci.* **134** (2021).
359 24 Bretschneider, T. *et al.* The three-dimensional dynamics of actin waves, a model
360 of cytoskeletal self-organization. *Biophys. J.* **96**, 2888-2900 (2009).
361 25 Zhang, K., Lyu, W., Yu, J. & Koleske, A. J. Abl2 is recruited to ventral actin
362 waves through cytoskeletal interactions to promote lamellipodium extension.
363 *Mol. Biol. Cell* **29**, 2863-2873 (2018).
364 26 Ruthel, G. & Banker, G. Actin-dependent anterograde movement of
365 growth-cone-like structures along growing hippocampal axons: a novel form of
366 axonal transport? *Cell Motil. Cytoskelet.* **40**, 160-173 (1998).
367 27 Parker, K. K. *et al.* Directional control of lamellipodia extension by constraining
368 cell shape and orienting cell tractional forces. *FASEB J.* **16**, 1195-1204 (2002).
369 28 Koestler, S. A., Auinger, S., Vinzenz, M., Rottner, K. & Small, J. V.
370 Differentially oriented populations of actin filaments generated in lamellipodia
371 collaborate in pushing and pausing at the cell front. *Nat. Cell Biol.* **10**, 306-313
372 (2008).
373 29 Gerisch, G. *et al.* Mobile actin clusters and traveling waves in cells recovering
374 from actin depolymerization. *Biophys. J.* **87**, 3493-3503 (2004).
375 30 Hadjitheodorou, A. *et al.* Directional reorientation of migrating neutrophils is
376 limited by suppression of receptor input signaling at the cell rear through myosin
377 II activity. *Nat. Commun.* **12**, 6619 (2021).
378 31 Xiong, Y., Huang, C. H., Iglesias, P. A. & Devreotes, P. N. Cells navigate with a
379 local-excitation, global-inhibition-biased excitable network. *Proc. Natl. Acad.*
380 *Sci. U. S. A.* **107**, 17079-17086 (2010).
381 32 Yamada, K. M. & Sixt, M. Mechanisms of 3D cell migration. *Nat. Rev. Mol.*
382 *Cell Biol.* **20**, 738-752 (2019).

33 Jasnin, M., Ecke, M., Baumeister, W. & Gerisch, G. Actin organization in cells responding to a perforated surface, revealed by live imaging and cryo-electron tomography. *Structure* **24**, 1031-1043 (2016).

34 Hadjitheodorou, A. *et al.* Leading edge competition promotes context-dependent responses to receptor inputs to resolve directional dilemmas in neutrophil migration. *Cell Syst.* **14**, 196-209 e196 (2023).

35 Paoluzzi, M., Di Leonardo, R., Marchetti, M. C. & Angelani, L. Shape and displacement fluctuations in soft vesicles filled by active particles. *Sci. Rep.* **6**, 34146 (2016).

36 Li, Y. & Ten Wolde, P. R. Shape transformations of vesicles induced by swim pressure. *Phys. Rev. Lett.* **123**, 148003 (2019).

37 Boudet, J. F. *et al.* From collections of independent, mindless robots to flexible, mobile, and directional superstructures. *Sci. Robot.* **6** (2021).

38 Huber, L., Suzuki, R., Kruger, T., Frey, E. & Bausch, A. R. Emergence of coexisting ordered states in active matter systems. *Science* **361**, 255-258 (2018).

39 Mallavarapu, A. & Mitchison, T. Regulated actin cytoskeleton assembly at filopodium tips controls their extension and retraction. *J. Cell Biol.* **146**, 1097-1106 (1999).

40 Suter, D. M. & Forscher, P. Substrate-cytoskeletal coupling as a mechanism for the regulation of growth cone motility and guidance. *J. Neurobiol.* **44**, 97-113 (2000).

41 Tatavarty, V., Kim, E. J., Rodionov, V. & Yu, J. Investigating sub-spine actin dynamics in rat hippocampal neurons with super-resolution optical imaging. *PLoS ONE* **4**, e7724 (2009).

42 Lin, W. H., Nebhan, C. A., Anderson, B. R. & Webb, D. J. Vasodilator-stimulated phosphoprotein (VASP) induces actin assembly in dendritic spines to promote their development and potentiate synaptic strength. *J. Biol. Chem.* **285**, 36010-36020 (2010).

43 Loomis, P. A. *et al.* Espin cross-links cause the elongation of microvillus-type parallel actin bundles in vivo. *J. Cell Biol.* **163**, 1045-1055 (2003).

44 Meenderink, L. M. *et al.* Actin dynamics drive microvillar motility and clustering during brush border assembly. *Dev. Cell* **50**, 545-556 e544 (2019).

45 Kovacs, E. M. *et al.* N-WASP regulates the epithelial junctional actin cytoskeleton through a non-canonical post-nucleation pathway. *Nat. Cell Biol.* **13**, 934-943 (2011).

46 Efimova, N. & Svitkina, T. M. Branched actin networks push against each other at adherens junctions to maintain cell-cell adhesion. *J. Cell Biol.* **217**, 1827-1845 (2018).

47 Rzadzinska, A. K., Schneider, M. E., Davies, C., Riordan, G. P. & Kachar, B. An actin molecular treadmill and myosins maintain stereocilia functional architecture and self-renewal. *J. Cell Biol.* **164**, 887-897 (2004).

48 Oser, M. *et al.* Cortactin regulates cofilin and N-WASp activities to control the stages of invadopodium assembly and maturation. *J. Cell Biol.* **186**, 571-587 (2009).

49 Albiges-Rizo, C., Destaing, O., Fourcade, B., Planus, E. & Block, M. R. Actin machinery and mechanosensitivity in invadopodia, podosomes and focal adhesions. *J. Cell Sci.* **122**, 3037-3049 (2009).

50 Gerisch, G. Self-organizing actin waves that simulate phagocytic cup structures. *PMC Biophys.* **3**, 7 (2010).

51 Okano, K. *et al.* In situ laser micropatterning of proteins for dynamically arranging living cells. *Lab Chip* **13**, 4078-4086 (2013).

52 Baba, K. *et al.* Gradient-reading and mechano-effector machinery for netrin-1-induced axon guidance. *eLife* **7**, e34593 (2018).

53 Toriyama, M. *et al.* Shootin1: A protein involved in the organization of an asymmetric signal for neuronal polarization. *J. Cell Biol.* **175**, 147-157 (2006).

54 Higashiguchi, Y. *et al.* Identification of a shootin1 isoform expressed in peripheral tissues. *Cell Tissue Res.* **366**, 75-87 (2016).

55 Cameron, L. A., Robbins, J. R., Footer, M. J. & Theriot, J. A. Biophysical parameters influence actin-based movement, trajectory, and initiation in a cell-free system. *Mol. Biol. Cell* **15**, 2312-2323 (2004).

56 Kalwarczyk, T. *et al.* Comparative analysis of viscosity of complex liquids and cytoplasm of mammalian cells at the nanoscale. *Nano Lett.* **11**, 2157-2163 (2011).

447 **Methods**

448 **Cell culture and transfection**

449 A subline of glioma U251 cells[17] and COS7 cells were seeded on glass-bottom dishes
450 (Matsunami, #D11130H) coated with 100 μg/ml poly-D-lysine (Sigma) and 5 μg/ml
451 laminin (Lonza), and cultured in DMEM high glucose medium (Nacalai, #08458-16)
452 supplemented with 10% fetal bovine serum (Japan Bio Serum) at 37°C and 5% CO_2.
453 They were transfected with vectors using Polyethylenimine MAX (PEI MAX,
454 Polysciences) following the manufacturer's protocol.

455

456 **Generation of shootin1b KO U251 cells by CRISPR-Cas9**

457 The guide oligonucleotide sequence (forward:
458 5′-CACCGGCAGCTCATTACCAGTCTGA-3′; reverse:
459 5′-AAACTCAGACTGGTAATGAGCTGCC-3′), corresponding to nucleotides 30-49 in
460 the coding region of human shootin1b, were selected by an online CRISPR Cas9 Design
461 tool (http://crispr.mit.edu/). The pSpCas9(BB)-2A-Puro (PX459) V2.0 plasmid
462 (Addgene, #62988) was linearised using by BbsI-HF (New England Biolabs, #R3539S),
463 then the guide oligonucleotides were annealed and inserted into the vector using
464 Ligation high Ver.2 (TOYOBO, #LGK-201). U251 cells were transfected with the
465 plasmid, cultured individually in 96-well plates, and screened using 4 μg/ml puromycin.
466 Shootin1b depletion in KO cells was confirmed by immunoblot analyses (Extended
467 Data Fig. 2g).

468

469 **Micropatterning of laminin on the substrate for cell adhesion**

470 Micropatterns of laminin for cell adhesion were produced on a glass surface following
471 our previously established procedure[51], with modifications (Extended Data Fig. 3a). The
472 glass-bottom dish (Iwaki, #3961-035) was cleaned using ultrasonic waves for 5 min
473 with special grade ethanol, followed by rinsing with water and additional 5-min
474 ultrasonic cleaning with pure water. After the cleaning, the dish was air-dried in a clean
475 room at room temperature. 3-Phenylaminopropyltrimethoxysilane (2%, Shin-Etsu,
476 #LS-4500) was dissolved in a 2% solution of acetic acid in water and then poured onto
477 the glass-bottom dish, followed by incubation for 30 min. After being washed twice
478 with water, the dish was dried at 70°C for 1 h. This process resulted in the covalent

479 bonding of the 3-phenylaminopropyl group with the glass surface, which made it
480 hydrophobic. Any residues resulting from the reaction were eliminated by ultrasonically
481 cleaning with special grade ethanol for 5 min.

482 The hydrophobic glass surface was coated with 100 µl of ethanol containing
483 0.2% of MPC (2-methacryloyloxyethyl phosphorylcholine) polymer (NOF,
484 #Lipiduro-CM5206). After the reaction for 10-15 sec, the coating solution was removed
485 and left to dry overnight at room temperature in the dark. This resulted in the formation
486 of an MPC polymer film on the glass. Then, the dish was incubated with 2 ml H_2O
487 overnight. In the film, the phosphatidylcholine residues of the MPC polymers are
488 oriented towards the aqueous solution (Extended Data Fig. 3a).

489 The cell non-adhesive MPC-polymer layer was removed by a programmed
490 raster scanning of a femtosecond laser (center wavelength 800 nm, pulse width 130 fs,
491 pulse energy 100 nJ, transmission frequency 5 kHz, Solstice, Spectra-Physics) focused
492 with an objective lens 20x 0.46 NA (Olympus, UMPlanFl) at a speed of 400 µm/s on
493 the glass surface. The raster scanning patterns are shown in Extended Data Fig. 3a, b.
494 Then, the cell-adhesive patterns of laminin were produced by coating the exposed glass
495 surface with poly-D-lysine (PDL) and laminin. The cell-adhesive patterns were
496 confirmed by coating with green fluorescent-HiLyte 488-Laminin (Cytoskeleton,
497 #LMN02-A) (Extended Data Fig. 3a).

498

499 **Immunocytochemistry**

500 Immunocytochemistry was performed as described previously[52]. Cultured cells were
501 fixed with 3.7% formaldehyde in Krebs buffer (118 mM NaCl, 4.7 mM KCl, 1.2 mM
502 KH_2PO_4, 1.2 mM $MgSO_4$, 4.2 mM $NaHCO_3$, 2 mM $CaCl_2$, 10 mM glucose, 400 mM
503 sucrose, 10 mM HEPES pH 7.0) for 20 min on ice and 10 min at room temperature,
504 followed by treatment for 15 min with 0.05% Triton X-100 in PBS on ice and 10% fetal
505 bovine serum in PBS for 1 h at room temperature. The cells were incubated with a
506 primary antibody diluted in PBS containing 10% fetal bovine serum overnight at 4°C.
507 They were washed with PBS, and then incubated with secondary antibody diluted in
508 PBS for 1 h at room temperature. After washing with PBS, the cells were stained with
509 Alexa Fluor 594 conjugated phalloidin (1:100, Thermo Fisher Scientific) and DAPI
510 (1:1000, Thermo Fisher Scientific) for 30 min at room temperature. The fluorescence

511 and phase-contrast images of U251 cells were acquired a fluorescence microscope (Carl
512 Zeiss, Axioplan2) equipped with an objective lens 40x 0.75 NA (Carl Zeiss,
513 plan-Neofluar), a charge-coupled device camera (Carl Zeiss, AxioCam MRm) and
514 imaging software (Carl Zeiss, ZEN), and a TIRF microscope (Olympus, IX81) equipped
515 with a CMOS camera (Hamamatsu, ORCA Flash4.0LT), an objective lens 100x 1.49
516 NA (Olympus, UAPON), and MetaMorph software.
517
518 **Immunoblot**
519 Cultured U251 cells were lysed with RIPA buffer (50 mM Tris-HCl (pH 8.0), 1 mM
520 EDTA, 150 mM NaCl, 1% Triton X-100, 0.1% SDS, 0.1% sodium deoxycholate, 1 mM
521 DTT, 1 mM PMSF, and 0.01 mM leupeptin), and incubated for 10 min at 4°C.
522 Subsequently, the cell lysate was centrifuged at 15000 rpm for 15 min at 4°C. The
523 supernatant was mixed with an equal volume of 2 x SDS sample buffer (131 mM
524 Tris-HCl, pH 6.8, 21% glycerol, 4% SDS, 0.05% bromophenol blue and 5%
525 β-mercaptoethanol). The mixture was incubated for 5 min at 95°C, followed by
526 SDS-polyacrylamide gel electrophoresis. Immunoblotting was performed as described
527 previously[21].
528
529 **Antibodies**
530 The following primary antibodies were used: anti-shootin1 (rabbit, 1:400)[53];
531 anti-shootin1b (rabbit, 1:2000)[54]; anti-NCAM-L1 (mouse, 1:1000, Santa Cruz
532 Biotechnology, #sc-514360); anti-cortactin (mouse, 1:1000, Millipore, #05-180);
533 anti-actin (mouse, 1:1000, Millipore, #MAB1501R); anti-ARPC2 (rabbit, 1:1000,
534 Millipore, #07-227). The following secondary antibodies were used: anti-rabbit (Alexa
535 594 conjugated donkey, 1:1000, Jackson ImmunoResearch Labs, #711-585-152);
536 anti-rabbit (Alexa 488 conjugated goat, 1:1000, Thermo Fisher Scientific, #A-11008);
537 anti-mouse (Alexa 488 conjugated goat, 1:1000, Thermo Fisher Scientific, #A-11029);
538 anti-rabbit (HRP conjugated donkey, 1:2000, GE Healthcare, #NA934); anti-mouse
539 (HRP conjugated goat, 1:5000, Thermo Fisher Scientific, #AP308P).
540
541 **Chemicals**
542 The following reagents were used: phalloidin (Alexa Fluor 594 conjugated, 1:100,

543 Thermo Fisher Scientific, #A12381); DAPI (1:1000, Thermo Fisher Scientific,
544 #D1306); Poly-D-lysine (100 μg/ml, Sigma, #P6407-5MG); Laminin (5 μg/ml, Lonza,
545 #120-05751); HaloTag TMR ligand (5mM, Promega, #G8251); LIPIDURE (0.2% NOF,
546 #CM5206); 3-phenylaminopropyltrimethoxysilane (2%, Shin-Etsu, #LS-4500)
547
548 **DNA construction**
549 To generate pEGFP-N1-LifeAct vector, the annealed LifeAct (forward:
550 5′-TCGAGATGGGTGTCGCAGATTTGATCAAGAAATTCGAAAGCATCTCAAAG
551 GAAGAAGGG-3′; reverse:
552 5′-GATCCCTTCTTCCTTTGAGATGCTTTCGAATTTCTTGATCAAATCTGCGACA
553 CCCATC-3′) was fused to N-terminal of EGFP-N1 vectors (Clontech). To generate
554 pLifeAct-mCherry-N1 vector, the annealed LifeAct was fused to N-terminal of
555 mCherry-N1 vectors (Takara, #632523). Generation of pFN21A-HaloTag-actin was
556 described previously[21].
557
558 **TIRF and epifluorescence microscopy**
559 U251 cells were cultured on glass-bottom dishes coated with PDL and laminin. Actin
560 dynamics in close proximity to the ventral plasma membrane were visualised using the
561 actin filament marker EGFP-LifeAct or LifeAct-mCherry under TIRF or
562 epifluorescence microscopy. In addition, to differentially visualise actin waves
563 translocating in close proximity to the ventral plasma membrane and those detached
564 from the membrane, we combined TIRF microscopy, which visualises the region in
565 close proximity to the ventral plasma membrane, and epifluorescence microscopy,
566 which visualises the entire cell thickness (Extended Data Fig. 1e). U251 cells
567 expressing LifeAct-mCherry and EGFP-LifeAct were cultured on glass-bottom dishes
568 coated with PDL and laminin. Prior to observation, the cells were incubated in
569 DMEM/F-12 Ham medium (Sigma) supplemented with 10% FBS (Japan Bio Serum).
570 The TIRF laser was used to observe fluorescence images of LifeAct-mCherry, while the
571 epifluorescence laser was used to observe fluorescence images of EGFP-LifeAct. The
572 observations were made with a TIRF microscope (Olympus, IX81) equipped with a
573 CMOS camera (Hamamatsu, ORCA Flash4.0LT), an objective lens 100x 1.49 NA or

574 150x 1.45 NA (Olympus, UAPON), and MetaMorph software. Images were acquired
575 every 10 or 60 sec.
576
577 **Fluorescent speckle imaging of actin wave by TERF microscopy**
578 U251 cells expressing HaloTag-actin and EGFP-LifeAct were cultured on glass-bottom
579 dishes coated with PDL and laminin. Prior to observation, the cells were treated with
580 0.05 μM HaloTag TMR ligand (Promega) in the culture medium and incubated for 1 h
581 at 37°C. The ligand was washed with PBS, and the cells were then incubated in
582 DMEM/F-12 Ham medium (Sigma, #D8062) supplemented with 10% FBS (Japan Bio
583 Serum). The fluorescent speckles of HaloTag-actin and EGFP-LifeAct were observed
584 using a TIRF microscope (Olympus, IX81) equipped with a CMOS camera
585 (Hamamatsu, ORCA Flash4.0LT), an objective lens 150x 1.45 NA (Olympus, UAPON),
586 and MetaMorph software. Fluorescence images were acquired every 10 sec. Actin flow
587 velocity was calculated by tracing the speckles of HaloTag-actin in actin waves using
588 ImageJ (Fiji version). Actin polymerisation rate was calculated as the sum of actin wave
589 migration velocity, visualised by EGFP-LifeAct, and HaloTag-actin flow velocity, as
590 reported[18].
591
592 **3D imaging by confocal deconvolution microscopy**
593 U251 cells expressing HaloTag-actin and EGFP-LifeAct were cultured in 2D (on
594 glass-bottom dishes coated with PDL and laminin) or 3D (75% matrigel) environment.
595 Before observation, the cells were incubated with 0.05 μM HaloTag TMR ligand
596 (Promega) in the culture medium and incubated for 1 h at 37°C. The ligand was washed
597 with PBS, and the cells were then incubated in DMEM/F-12 Ham medium (Sigma)
598 supplemented with 10% FBS (Japan Bio Serum). The fluorescent speckles of
599 HaloTag-actin and EGFP-LifeAct were observed using a confocal microscope (Leica,
600 Stellaris 8) equipped with an objective lens 100x 1.40 NA (Leica, HC PL APO CS2) and
601 Las X software. Deconvolution of 3D image stacks were obtained by Las X software.
602
603 **Statistical analyses**
604 Statistical analyses were performed using Excel (Microsoft 365) or GraphPad Prism 7
605 (GraphPad Software). For samples with more than 7 data points, the D′Agostino–

606 Pearson normality test was used to determine whether the data followed a normal
607 distribution. In cases where the number of data points was between 3 and 7, the
608 Shapiro–Wilk test was used for the normality test. We also tested the equality of
609 variation with the F test for two independent groups that followed normal distributions.
610 Significance tests were performed as follows: (1) two-tailed unpaired Student′s *t*-test to
611 compare normally distributed data with equal variance from two independent groups;
612 (2) two-tailed unpaired Welch′s *t*-test to compare normally distributed data with unequal
613 variance from two independent groups; (3) two-tailed Mann–Whitney *U*-test to compare
614 nonnormally distributed data from two independent groups. The statistical information
615 and number of samples for each experiment are indicated in the Figure legends. For
616 detailed statistical results including the test statistics and exact p values, see the
617 statistical source data associated with each Figure. All data are shown as the mean ±
618 SEM. Statistical significance was defined as ***$p < 0.01$; **$p < 0.02$; *$p < 0.05$; ns, not
619 significant. All experiments were performed at least three times and reliably reproduced.
620 The investigators were blinded to the experimental groups for each analyses.
621
622 **Mathematical modelling**
623 To investigate whether actin waves mediate the accumulation of actin filaments at the
624 protrusions of cells confined to adhesive islands (Fig. 3c), we constructed a
625 mathematical model that describes the movement of intracellular actin waves. Our
626 model is based on quantitative data obtained from experimental observations: we
627 focused on filopodium-type waves because it is difficult to observe individual actin
628 filaments in lamellipodium-type waves (Fig. 1c), and filopodium-type and
629 lamellipodium-type waves are interchangeable (Extended Data Fig. 1c). For simplicity,
630 the present model describes the translocation of the actin filament arrays, not a detailed
631 mechanism of wave translocation[12]. The model depicts the processes of wave
632 emergence and disappearance, as well as changes in the direction of wave translocation.
633 The model parameters used in the model are summarised in Extended Data Table 1.
634
635 ***Emergence and disappearance of actin waves***
636 Our experimental data indicate that actin waves emerge widely in the cytoplasm, move
637 in random directions, and then disappear (Supplementary Video 1). In our model, the

638 emergence locations and translocation directions of actin waves are randomly chosen at
639 the start of the simulation. The simulation is updated every 1 sec (Δt = 1 sec),
640 generating one actin wave in the cell with a probability of 10%. The lifetimes of actin
641 waves in WT and shootin1b KO cells, quantified by live cell imaging, were modeled
642 using gamma distributions (Extended Data Fig. 4a, b).
643 The length (L) and translocation velocity (V) of actin waves are also derived
644 from experimental data (Extended Data Fig. 4e and Fig. 1i); the model uses their
645 average values for simplicity (Extended Data Table 1). Actin waves located at the cell
646 periphery move laterally along the cell membrane (Fig. 2d). The velocity of the lateral
647 movement was modelled as $\cos\theta$ of the mean velocity of actin waves (Fig. 1i), where θ
648 is the angle of the direction of wave movement with respect to the cell membrane (Fig.
649 2f).
650 The local concentration of actin subunits increases immediately after the
651 disappearance (complete disassembly) of actin wave. Since actin polymerisation
652 depends on the local concentration of actin subunits, our model assumes that an actin
653 wave reemerges at the location where the preceding wave disappeared and translocates
654 in a random direction.
655
656 ***Change in the direction of wave translocation***
657 Actin waves frequently change the direction of their translocation (Supplementary
658 Videos 1 and 4). The change in direction was quantified every 50 sec from live cell
659 imaging data (Extended Data Fig. 4d). As the angular distribution of these changes was
660 symmetric with a zero peak, we modelled it using a Gaussian distribution (Extended
661 Data Fig. 4d).
662
663 **Analyses of actin filament accumulation and lamellipodial formation**
664 Accumulation of actin filaments at the cell periphery was determined by dividing the
665 average fluorescence intensity of actin filaments within a 2 μm-wide region from the
666 cell periphery (green region, Extended Data Fig. 3c) by the average intensity of actin
667 filaments in the whole cell region (blue region). Accumulation of actin filaments at the
668 cell protrusions was determined by dividing the average intensity of actin filaments at
669 the corner regions (yellow region: 2 μm-wide and 5 μm-long regions in both sides of the

corner, Extended Data Fig. 3c) by the average intensity of actin filaments in the peripheral region (green region). Lamellipodial coverage rate was calculated by dividing the total length of lamellipodia (yellow line, Extended Data Fig. 5a) by the perimeter of the cell (green line). The fluorescence intensity of actin filaments was analysed using ImageJ (Fiji version). Lamellipodia was defined as the area of cell periphery where the fluorescence intensity exceeded the mean intensity + SD of the whole cell body. The polar histogram of the lamellipodial areas was generated using MATLAB (Fig. 4d).

Data availability

Data will be made available upon reasonable request.

Code availability

The MATLAB codes used for mathematical simulations are available at GitHub (https://github.com/KioYagami/actin-wave/tree/master). Any additional information will be available from the corresponding author upon reasonable request.

Acknowledgments

We thank Drs. Masatoshi Takeichi (Riken) and Shintaro Suzuki (Kwansei Gakuin Univ) for providing the subline of U251 cells, Drs. Hitoshi Sakano (Fukui Univ), Jim Bamburg (CSU), Nir Gov (Weizmann Inst Sci), Carsten Beta (Potsdam Univ), Sean Collins (UC Davis), Klemens Rottner (Tech Univ Braunschweig), Giovanni Volpe (Univ Gothenburg), Shiro Suetsugu (NAIST), Naoki Watanabe (Kyoto Univ) and Yusuke Maeda (Kyushu Univ) for valuable discussions, and Satoko Shimamura for kind encouragements. This research was supported in part by AMED under Grant Number JP17gm0810011 (N.I.), JSPS KAKENHI (JP19H03223, N.I.), JSPS Grants-in-Aid for Early-Career Scientists (JP19K16127, K.B. and JP23K14181, T.M.), and the Osaka Medical Research Foundation for Incurable Diseases (K.B., T.M.).

Author contributions

K.Y., K.B., S.M., H.K.-K. and K.O. performed the experiments and data analyses. K.Y., K.B., S.M., H.K.-K., T.M., K.O., Y.H. and N.I. designed the experiments. K.Y., Y.S. and N.I. constructed the mathematical model. K.Y., Y.S., K.O. and N.I. wrote the

manuscript. N.I. supervised all the projects. All authors discussed the results and commented on the manuscript.

Competing Interest Statement

The authors declare that they have no competing interests.

709 **Figure legends**

710 **Fig. 1. Actin waves emerge widely in cells and translocate by treadmilling. a**, A
711 fluorescence image of a U251 cell expressing EGFP-LifeAct obtained by TIRF
712 microscopy. Asterisk indicates cellular leading edge. See Supplementary Video 1. **b-c**,
713 Fluorescence time-lapse images of filopodium-type (arrowheads, **b**) and
714 lamellipodium-type (arrows, **c**) actin waves in U251 cells expressing LifeAct-mCherry
715 obtained by TIRF microscopy. **d-e**, Fluorescence time-lapse images of actin waves on
716 the dorsal membrane (blue arrowheads and arrows, **d**) and filopodium-type actin waves
717 in cytoplasm (green arrowheads, **e**) in U251 cells expressing LifeAct-mCherry obtained
718 by 3D imaging with confocal deconvolution microscopy. See Supplementary Video 5. **f**,
719 A fluorescent speckle image of HaloTag-actin in a U251 cell obtained by TIRF
720 microscopy; actin filaments were also monitored by EGFP-LifeAct. See Supplementary
721 Video 6. Time-lapse montages of a filopodium-type actin wave in the rectangular region
722 at 10-sec intervals are shown to the right. Green and magenta lines indicate wave
723 forward translocation and actin filament retrograde flow, respectively. Actin
724 polymerisation rate can be calculated as the sum of the forward translocation rate and
725 actin retrograde flow rate (double-headed arrow). **g**, A diagram showing the
726 translocation mechanisms of actin waves travelling on the ventral plasma membrane
727 (left)[12]. Right panels show a possible mode of actin wave translocation observed in **e**
728 and Extended Data Fig. 1f. For explanations, see text and Supplementary Discussion. **h**,
729 Translocation velocities of filopodium-type actin waves (**f**, green line) before and after
730 the application of DMSO (control, N = 4 cells: before application, n = 34 waves; after
731 application, n = 32 waves), CK666 (N = 3 cells: before application, n = 49 waves; after
732 application, n = 33 waves) or SMIFH2 (N = 5 cells: before application, n = 52 waves;
733 after application, n = 37 waves). **i**, Velocities of actin filament retrograde flow (**f**,
734 magenta line), actin filament polymerisation (**f**, double-headed arrow), and
735 filopodium-type wave translocation (**f**, green line) in WT and shootin1b KO U251 cells
736 (WT, N = 11 cells, n = 71 waves; KO#1, N = 9 cells, n = 69 waves; KO#2, N = 10 cells,
737 n = 45 waves). Scale bars, 20 μm (**a**); 5 μm (**f** left): 1 μm (**b**, **c**, **d**, **e**, **f** right). Data
738 represent means ± SEM; ***$p < 0.01$; *$p < 0.05$; ns, not significant. Statistical analyses
739 were performed using the two-tailed Mann–Whitney *U*-test (**h**, **i**).

740

741 **Fig. 2. Actin wave arrival at the periphery promotes membrane protrusion. a-b**,
742 Fluorescence time-lapse images of filopodium-type actin waves (arrowheads) which
743 entered into pre-existing lamellipodium (arrows, **a**) and filopodium (asterisks, **b**) in
744 U251 cells expressing EGFP-LifeAct obtained by TIRF microscopy. Entry of the waves
745 into lamellipodia resulted in local actin filament accumulation and lamellipodial
746 extension (arrows, **a**). See Supplementary Video 7. **c-d**, Fluorescence time-lapse images
747 of lamellipodium-type actin wave (yellow arrows, **c**) and filopodium-type actin waves
748 (arrowheads, **d**) which arrived at the cell periphery in U251 cells expressing
749 LifeAct-mCherry obtained by TIRF microscopy (**c**) and expressing EGFP-LifeAct
750 obtained by epifluorescence microscopy (**d**). They pushed the plasma membrane,
751 resulting in the formation of lamellipodium (**c**) and filopodia (**d**), and continued to move
752 laterally along the membrane. The former merged with the pre-existing lamellipodium
753 (blue arrows, **d**). See Supplementary Videos 8 and 9. **e**, A diagram describing the
754 relationship between the velocities of lateral movement (V_L) and ventral movement (V_V)
755 of filopodium-type actin waves. If actin waves move laterally along the membrane
756 driven by directional actin treadmilling, V_L is equal to $V_V \cos\theta$, where θ is the angle of
757 the polymerising actin filaments with respect to the membrane. **f**, Fluorescence
758 time-lapse images of a filopodium-type actin wave travelling along the lateral
759 membrane (arrowheads) of a U251 cell expressing LifeAct-mCherry obtained by
760 epifluorescence microscopy. See Supplementary Video 10. The right graph shows V_L
761 and θ obtained by the time-lapse imaging; V_L closely matched $V_V\cos\theta$ (N = 10 cells, n =
762 21 waves). Scale bars, 5 μm (**c**, **d**, **f**); 1 μm (**a**, **b**).
763
764 **Fig. 3. Treadmilling actin waves spontaneously accumulate at cell protrusions. a-b**,
765 Fluorescence time-lapse images of filopodium-type (arrowheads, **a**) and
766 lamellipodium-type (arrows, **b**) actin waves which accumulated in protrusive regions
767 (asterisks) in U251 cells expressing EGFP-LifeAct obtained by epifluorescence
768 microscopy. See Supplementary Videos 11. **c**, A U251 cell cultured on a laminin-coated
769 triangular adhesive island and stained with Alexa Fluor 594 conjugated phalloidin (for
770 actin filament), anti-ARPC2 antibody, and DAPI (for nucleus). **d**, Fluorescence
771 time-lapse images of a U251 cell expressing LifeAct-mCherry obtained by
772 epifluorescence microscopy and cultured on a triangular adhesive island. Arrowheads

773 indicate an actin wave travelled along the lateral membrane, resulting in a local
774 accumulation of actin filaments at the corner upon arrival. See Supplementary Video 12.
775 **e-f**, Mathematical model data showing actin wave localisation in a triangular cell (**e**)
776 and cells with different corner angles, 30º, 60º, 120º or 180º (**f**), presented in arbitrary
777 unit (a.u.). See Supplementary Video 13. The right graph in **f** shows quantitative data for
778 the actin wave accumulation at the corners with different corner angles (30-180º, n = 20
779 simulations). **g**, U251 cells cultured on laminin-coated adhesive islands with the
780 different corner angles and stained with Alexa Fluor 594 conjugated phalloidin and
781 DAPI. The right graph shows quantitative data for the actin filament accumulation at the
782 corners (30º, N = 6 experiments, n = 22 cells; 60º, N = 8 experiments, n = 23 cells; 120º,
783 N = 7 experiments, n = 26 cells; 180º, N = 8 experiments, n = 18 cells). **h**, Mathematical
784 model data showing actin wave localisation in a triangular shootin1b KO cell. See
785 Supplementary Video 13. The right graphs show quantitative data for actin wave
786 accumulation at the edge and corners of WT and shoootin1b KO cells (WT, KO, n = 20
787 simulations). **i**, Shootin1b KO#1 U251 cells cultured on laminin-coated triangular
788 adhesive islands and stained with Alexa Fluor 594 conjugated phalloidin and DAPI. The
789 right graphs show quantitative data for actin filament accumulation at the edge and
790 corners of WT and shoootin1b KO cells (WT, N = 3 experiments, n = 13 cells; KO#1, N
791 = 6 experiments, n = 11 cells). Scale bars, 20 μm (**b**, **c**, **d**, **g**, **i**); 5 μm (**a**). Data represent
792 means ± SEM; ***p < 0.01; **p < 0.02; *p < 0.05; ns, not significant. Statistical
793 analyses were performed using the two-tailed unpaired Student′s *t*-test (**f**; 180º vs 120º,
794 120º vs 60º) (**g**; 180º vs 120º) (**h**, **i** right), two-tailed unpaired Welch′s *t*-test (**f**; 60º vs
795 30º) (**i** left), two-tailed Mann–Whitney *U*-test (**g**; 120º vs 60º, 60º vs 30º**)**.
796
797 **Fig. 4. Actin waves drive cell polarisation and migration. a**, WT, shootin1b KO#1
798 and KO#2 U251 cells stained with Alexa Fluor 594 conjugated phalloidin and DAPI.
799 **b-c**, Lamellipodial coverage rate (**b**) and histogram of lamellipodia localisation at cell
800 periphery (**c**) of WT, shootin1b KO#1 and KO#2 U251 cells in **a** (WT, KO#1, KO#2, N
801 = 3 experiments, n = 35 cells). **d-e**, Fluorescence time-lapse images of WT (**d**) and
802 shootin1b KO#1 (**e**) U251 cells expressing LifeAct-mCherry obtained by
803 epifluorescence microscopy: lower panels in (**d**) indicate enlarged time-lapse images of

804 the areas indicated by the dashed yellow boxes 1 and 2. The images were taken before
805 and after the treatment with 100 nM latrunculin A (Lat A), and at the indicated times
806 after the Lat A washout. The asterisks indicate foci of actin filament-enriched
807 protrusions. Yellow and blue arrows indicate enlargement and lateral expansions of
808 actin filament-enriched protrusions, respectively. See Supplementary Video 14. **f**,
809 Time-lapse phase-contrast images of WT and shootin1b KO#1 U251 cells taken after
810 the treatment with 100 nM Lat A and at the indicated times after the Lat A washout.
811 Yellow boxes trace cell movement. The right graph indicates the time required to start
812 cell migration after the Lat A washout (WT, N = 3 experiments, n = 28 cells; KO#1, N =
813 3 experiments, n = 40 cells; KO#2, N = 3 experiments, n = 35 cells). Scale bars, 20 μm
814 (**a**, **d**, **e**, **f**); 5 μm (**c**, **d** enlarged views). Data represent means ± SEM; ***p < 0.01; **p
815 < 0.02; *p < 0.05; ns, not significant. Statistical analyses were performed using the
816 two-tailed unpaired Student′s *t*-test (**b**; KO#1 vs KO#2), two-tailed unpaired Welch′s
817 t-test (**b**; WT vs KO#1, WT vs KO#2), two-tailed Mann–Whitney *U*-test (**f**).
818
819 **Fig. 5. A model of cell morphogenesis driven by self-propelled actin waves. a**, The
820 shape-guided actin filament accumulation through actin waves (green arrow) constitutes
821 a positive feedback interaction (red box) with actin-mediated cell protrusion, thereby
822 conferring robustness to the classical pathway of cell morphogenesis (black arrows),
823 under the regulation of signalling (blue arrow). This system can respond to extracellular
824 topographic cues that deform the plasma membrane from outside (yellow arrow). **b**, In
825 the LEGI model, a local activator of protrusion generates a global inhibitor (e.g. a
826 molecule or membrane tension) to suppress protrusion at the lateral regions (blue dotted
827 lines). The inhibitor would decay during the lateral propagation either by molecular
828 diffusion or by membrane stretching; it would also inhibit the activated area, hampering
829 the specific inhibition in the lateral regions (blue line). **c**, The self-propelled model does
830 not require a global inhibitor because the translocation of the activator (actin wave) to
831 the protrusion results in its lateral decrease, thereby suppressing protrusive activities
832 laterally (blue arrows). Thus, this model offers a simple framework of effective lateral
833 inhibition for cell morphogenesis (blue line).

834 **Supplementary Information**

835

836 **Supplementary Discussion**

837 **Translocation of treadmilling actin waves without anchoring to the plasma**
838 **membrane**

839 As we previously reported in axonal shafts[12], the present study demonstrates that actin
840 waves translocate through their treadmilling and anchoring to the ventral plasma
841 membrane and adhesive substrate (Fig. 1g, left). However, we also observed actin
842 waves travelling apart from the adhesive substrate (arrowheads, Extended Data Fig. 1f,
843 Supplementary Video 4) as well as those moving along the dorsal plasma membrane
844 (Fig. 1d) and within the cytoplasm without interacting with the plasma membrane (Fig.
845 1e, Supplementary Video 5). In addition, inhibition of actin filament anchorage to the
846 plasma membrane by shootin1b KO did not completely inhibit wave translocation.
847 Given the highly viscous cytoplasmic environments containing cytoskeletal components
848 [55,56], we propose that actin waves can translocate by treadmilling without anchoring to
849 the membrane when retrograde actin filament flow is mechanically obstructed in
850 viscous intracellular environments (Fig. 1g, right). This mechanism could also explain
851 the actin waves moving on the ventral plasma membrane, with polymerising actin
852 filaments oriented to the membrane[33].

853

854 **Extended Data Fig. 1. a**, A U251 cell stained with Alexa Fluor 594 conjugated
855 phalloidin. An enlarged view of the rectangular region is shown to the right. Arrows and
856 arrowheads indicate lamellipodia and filopodia, respectively. **b**, Time-lapse
857 phase-contrast images of U251 cells. **c**, Fluorescence time-lapse images of
858 filopodium-type (arrowheads) and lamellipodium-type (arrows) actin waves in U251
859 cells expressing LifeAct-mCherry obtained by TIRF microscopy. See Supplementary
860 Video 2. **d**, A fluorescence image of a COS7 cell expressing LifeAct-mCherry obtained
861 by TIRF microscopy: right panels indicate enlarged time-lapse images in rectangular
862 regions 1 and 2. Arrows and arrowheads indicate lamellipodium-type and
863 filopodium-type waves, respectively. See Supplementary Video 3. **e-f**, Fluorescence
864 time-lapse images of a U251 cell expressing LifeAct-mCherry (obtained by TIRF
865 microscopy) and EGFP-LifeAct (obtained by epifluorescence microscopy): lower

panels and **f** indicate enlarged time-lapse images in rectangular regions 1, 2 and 3. See Supplementary Video 4. Scale bars, 20 μm (**a**, **b**, **d**); 5 μm (**a**, **d** enlarged views, **c**, **e**); 1 μm (**e** enlarged views, **f**).

Extended Data Fig. 2. a, A Fluorescent speckle image of HaloTag-actin in a U251 cell obtained by TIRF microscopy; actin filaments were also monitored by EGFP-LifeAct. **b**, A Fluorescent speckle image of HaloTag-actin in a U251 cell obtained by 3D imaging with confocal deconvolution microscopy; actin filaments were also monitored by EGFP-LifeAct. **c**, Immunoblot analyses of U251 cells with anti-shootin1b, anti-cortactin and anti-L1 antibodies. **d**, A fluorescence image of a U251 cell stained with anti-shootin1b antibody, Alexa Fluor 594 conjugated phalloidin (for actin filament), and DAPI (for nucleus). **e**, A fluorescence image of a U251 cell stained with anti-shootin1b antibody and Alexa Fluor 594 conjugated phalloidin (for actin filament) obtained by TIRF microscopy. An enlarged view of the area within the rectangle is shown in the right panel. Arrowheads indicate shootin1b colocalisation with actin filament. **f**, Translocation velocities of filopodium-type actin waves before and after the application of 0.05 μM cytochalasin B (N = 4 cells, before application: n = 34 waves, after application: n = 28 waves). **g**, Immunoblot analysis of shootin1b in WT U251 cells, postnatal day 1 rate brain, and shootin1b KO U251 cells. The cell and tissue lysates were immunoblotted with anti-shootin1 and anti-actin antibodies. The arrowhead and asterisk indicate the bands corresponding to shootin1b and shootin1a, respectively. Shootin1a is a splicing variant of shootin1b expressed in neurons. Immunoblots with anti-actin antibody served as loading controls. **h**, A diagram showing the effects of shootin1b KO on the velocities of actin filament retrograde flow (magenta arrows) and actin wave translocation (green arrows). Scale bars, 20 μm (**b** left, **d**, **e** left); 5 μm (**b** middle, **e** right); 1 μm (**a**, **b** right). Data represent means ± SEM; ***$p < 0.01$. Statistical analyses were performed using the two-tailed Mann–Whitney U-test (**f**).

Extended Data Fig. 3. a, We created a triangular pattern of adhesive laminin substrate with the edge length 35 μm and the area 530.4 μm^2. The cell-adhesive patterns generated were confirmed by coating with green fluorescent-HiLyte 488-Laminin (see Methods). **b**, The pattern of adhesive laminin substrate with different corner angles, 30º,

60º, 120º or 180º, and the same width 23.8 μm and the same area 530.4 μm^2 used in the experiments in Fig. 3g, **c**, The accumulation of actin filaments at the cell periphery was determined by dividing the average actin intensity in the periphery (2 μm width) by the average actin intensity in the whole cell region. Similarly, the accumulation at corners was determined by dividing the average of actin intensity in the corner regions (2 μm width, 5 μm length) by the average actin intensity in the periphery. **d-e**, The accumulation rates of actin filaments at cell periphery in simulations (**d**, n = 20) and experiments (**e**, N = 3 experiments, n = 13 cells). Scale bars, 20 μm (**c**). Data represent means ± SEM.

Extended Data Fig. 4. Quantitative experimental data used in the model parameters. a-b, Distribution of the lifetime of filopodium-type waves in WT (**a**) and shootin1b KO#1 U251 cells (**b**). White bars indicate the experimental data in Fig. 1i, while red curves show gamma distributions with order $\boldsymbol{\alpha}$ = 3.0 and $\boldsymbol{\beta}$ = 119 (**a**; WT), and with $\boldsymbol{\alpha}$ = 2.4 and $\boldsymbol{\beta}$ = 106 (**b**; shootin1b KO#1). The parameters were chosen to give the best fit to the experimental data by maximum likelihood estimation. **c**, Lifetime of filopodium-type waves in WT and shootin1b KO#1 U251 cells (WT, KO#1, N = 9 cells, n = 100 waves). **d**, Distribution of the degree of the change in travelling direction of filopodium-type waves in 50 sec. White bars indicate the experimental data, while red curves show Gaussian distributions with order mean; $\boldsymbol{\mu}$ = -0.61 and SD; $\boldsymbol{\sigma}$ = 11. The parameters were chosen to give the best fit to the experimental data by maximum likelihood estimation (N = 8 cells, n = 86 waves). **e**, Length of filopodium-type waves (N = 4 cells, n = 40 waves). Data represent means ± SEM; ***$p < 0.01$. Statistical analysis was performed using the two-tailed Mann–Whitney U-test (**c**).

Extended Data Fig. 5. a, The lamellipodial coverage rate was determined by dividing the total length of lamellipodia (yellow line) by the perimeter of the cell (green line). **b**, Filopodium length of WT and shootin1b KO#1 U251 cells (WT, N = 6 cells, n = 51 filopodia; KO#1, N = 7 cells, n = 58 filopodia).

Extended Data Fig. 6. A model for cell polarisation and migration of U251 cells mediated by actin waves. The arrival of treadmilling actin waves at the cell periphery

(green arrows) aligns randomly oriented actin filaments towards outward polymerisation, which in turn pushes the membrane to protrude (white arrows). Shootin1b facilitates this process by mechanically coupling treadmilling actin filaments and the adhesive substrate[21]. Actin waves accumulate spontaneously at cell protrusions (red arrows), leading to their further enlargement. Through lateral expansion (yellow arrow), multiple protrusions are integrated into a large leading edge of the front. These processes work together with other mechanisms, such as myosin II-mediated contraction at the rear[17,30], to polarise cells and drive cell migration.

Extended Data Table 1. Model parameters estimated from experimental data.

Parameter	Value	Description	Figure
α	3.0 (WT) 2.4 (KO#1)	Parameters of the gamma distribution representing lifetime variation; estimated from quantitative data.	Extended Data Fig. 4a, b
β (sec)	119 (WT) 106 (KO#1)		
L (μm)	4.1	Actin wave length.	Extended Data Fig. 4e
V (μm/min)	2.0 (WT) 1.5 (KO#1)	Translocation velocity of actin wave.	Fig. 1i
μ, σ (degree)	$-0.61, 11$	Parameters of the Gaussian distribution representing actin wave directional change; quantified from experimental data.	Extended Data Fig. 4d

Legends for Supplementary Videos

Supplementary Video 1

A U251 cell expressing EGFP-LifeAct observed by TIRF microscopy. Filopodium-type and lamellipodium-type actin waves emerged widely in the cytoplasm, moved in random directions, and disappeared (see Fig. 1a). Time interval: 10 sec.

Supplementary Video 2

A Fluorescence time-lapse movie showing the interchangeability of filopodium-type (arrowheads) and lamellipodium-type (arrows) actin waves. A U251 cell expressing LifeAct-mCherry was observed by TIRF microscopy (see Extended Data Fig. 1c). Time interval: 60 sec.

Supplementary Video 3

Actin waves moving on the ventral plasma membrane of a COS7 cell expressing LifeAct-mCherry observed by TIRF microscopy (see Extended Data Fig. 1d). Time

interval: 60 sec.

Supplementary Video 4

A U251 cell expressing LifeAct-mCherry observed by TIRF microscopy and EGFP-LifeAct observed by epifluorescence microscopy. Actin waves observed by epifluorescence microscopy and TIRF microscopy are indicated by green and magenta arrowheads, respectively (see Extended Data Fig. 1e, f). Time interval: 60 sec.

Supplementary Video 5

An actin wave translocating through the cytoplasm without interacting with the plasma membrane (see Fig. 1e). A U251 cell expressing LifeAct-mCherry was observed by 3D imaging with confocal deconvolution microscopy. Time interval: 13 sec. Z-stack interval: 0.2 μm.

Supplementary Video 6

Fluorescent speckle dynamics of HaloTag-actin in a U251 cell observed by TIRF microscopy; actin filaments were also monitored by EGFP-LifeAct. The actin wave underwent treadmilling and translocated in the direction of polymerisation (see Fig. 1f). A Time interval: 10 sec.

Supplementary Video 7

Filopodium-type actin waves entering into pre-existing lamellipodium and filopodium. The wave entry resulted in local actin filament accumulation and lamellipodial expansion (see Fig. 2a, b). U251 cells expressing EGFP-LifeAct were observed by TIRF microscopy. Time interval: 10 sec.

Supplementary Video 8

Lamellipodium formation by a lamellipodium-type actin wave (see Fig. 2c). A U251 cell expressing LifeAct-mCherry was observed by TIRF microscopy. Time interval: 60 sec.

Supplementary Video 9

Filopodia formation by filopodium-type actin waves (see Fig. 2d). A U251 cell expressing EGFP-LifeAct was observed by epifluorescence microscopy. Time interval: 10 sec.

Supplementary Video 10

Filopodium-type actin waves travelling along the lateral membranes (see Fig. 2f). U251 cells expressing LifeAct-mCherry were observed by epifluorescence microscopy. Time interval: 10 sec.

Supplementary Video 11

Filopodium-type and lamellipodium-type actin waves accumulating at protrusive regions (see Fig. 3a, b). U251 cells expressing EGFP-LifeAct were observed by epifluorescence microscopy. Time interval: 10 sec.

Supplementary Video 12

Actin wave accumulation at the corners of a triangular U251 cell (see Fig. 3d). A U251 cell expressing LifeAct-mCherry was cultured on a triangular adhesive island and observed by epifluorescence microscopy. Time interval: 300 sec.

Supplementary Video 13

Simulation of actin wave accumulation in WT and shootin1b KO triangular cells (see Fig. 3e and h). All the model parameters are provided by our quantitative experimental data (see Extended Data Fig. 4, Extended Data Table 1). Time interval: 10 sec.

Supplementary Video 14

Fluorescence time-lapse movies of WT and shootin1b KO#1 U251 cells expressing LifeAct-mCherry and observed by epifluorescence microscopy. The images were taken before and after the treatment with 100 nM latrunculin A, and after the Lat A washout. Time interval: 60 sec.

Fig. 1 Yagami et al.

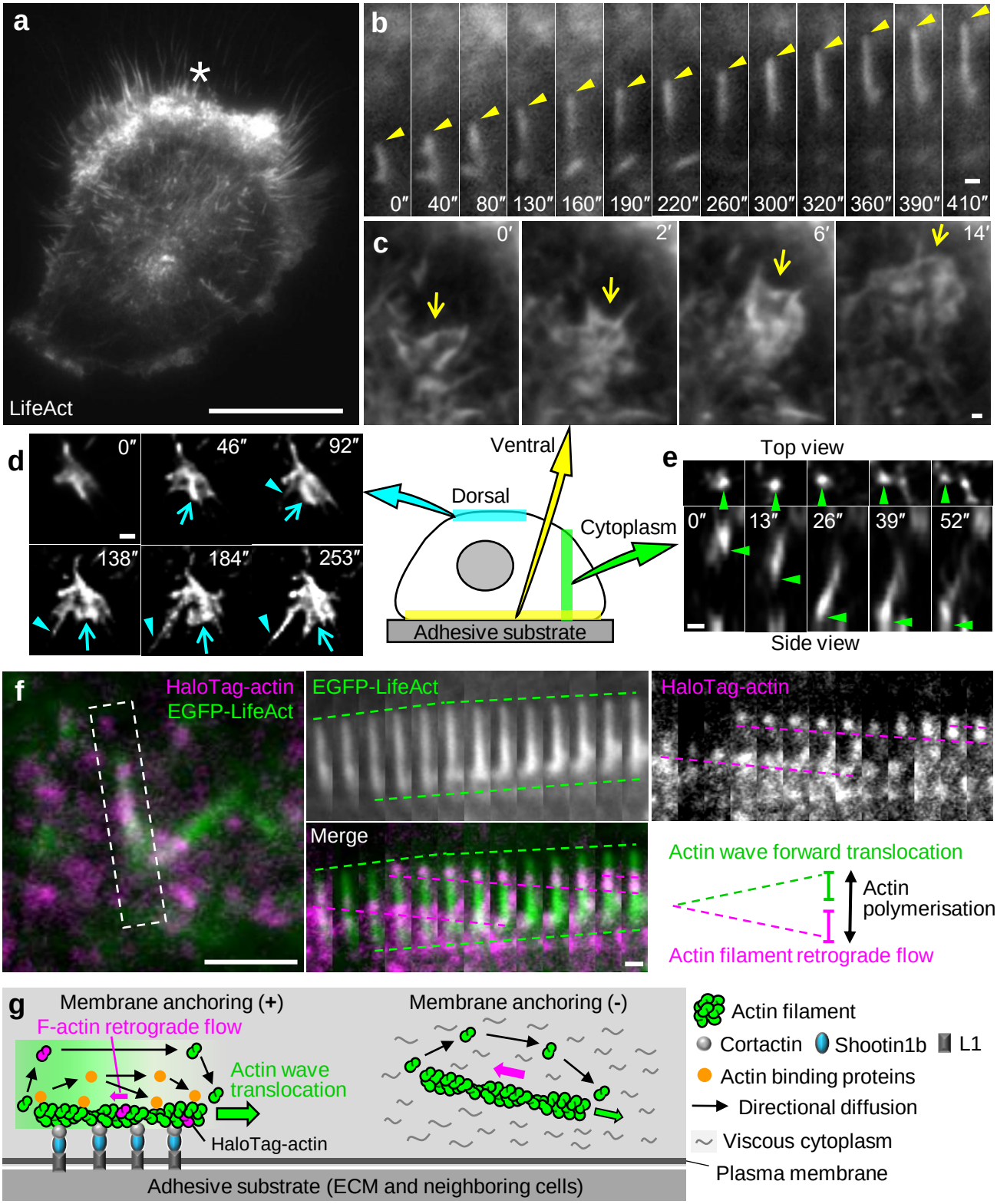

Fig. 2 Yagami et al.

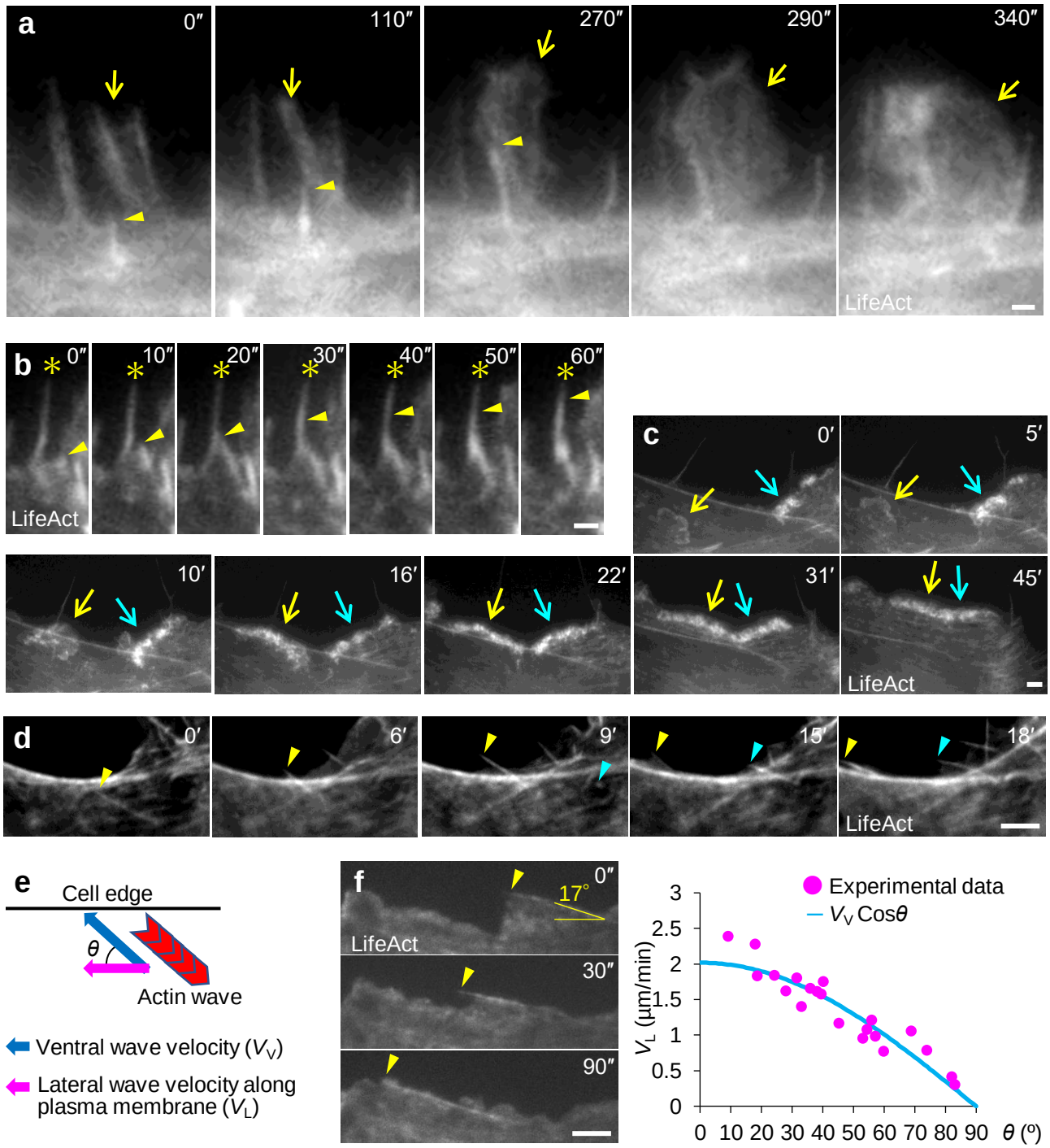

Fig. 3 Yagami et al.

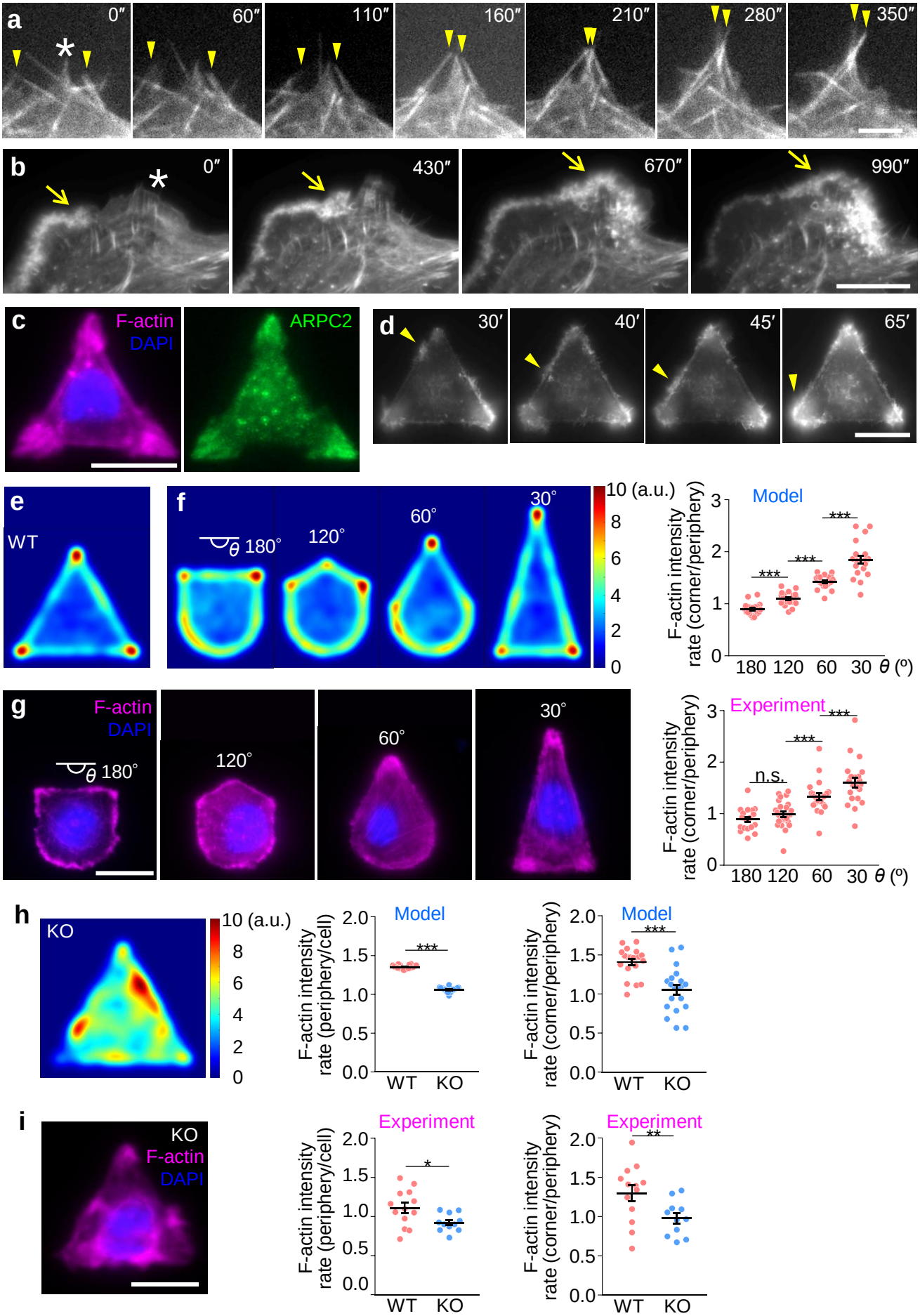

Fig. 4 Yagami et al.

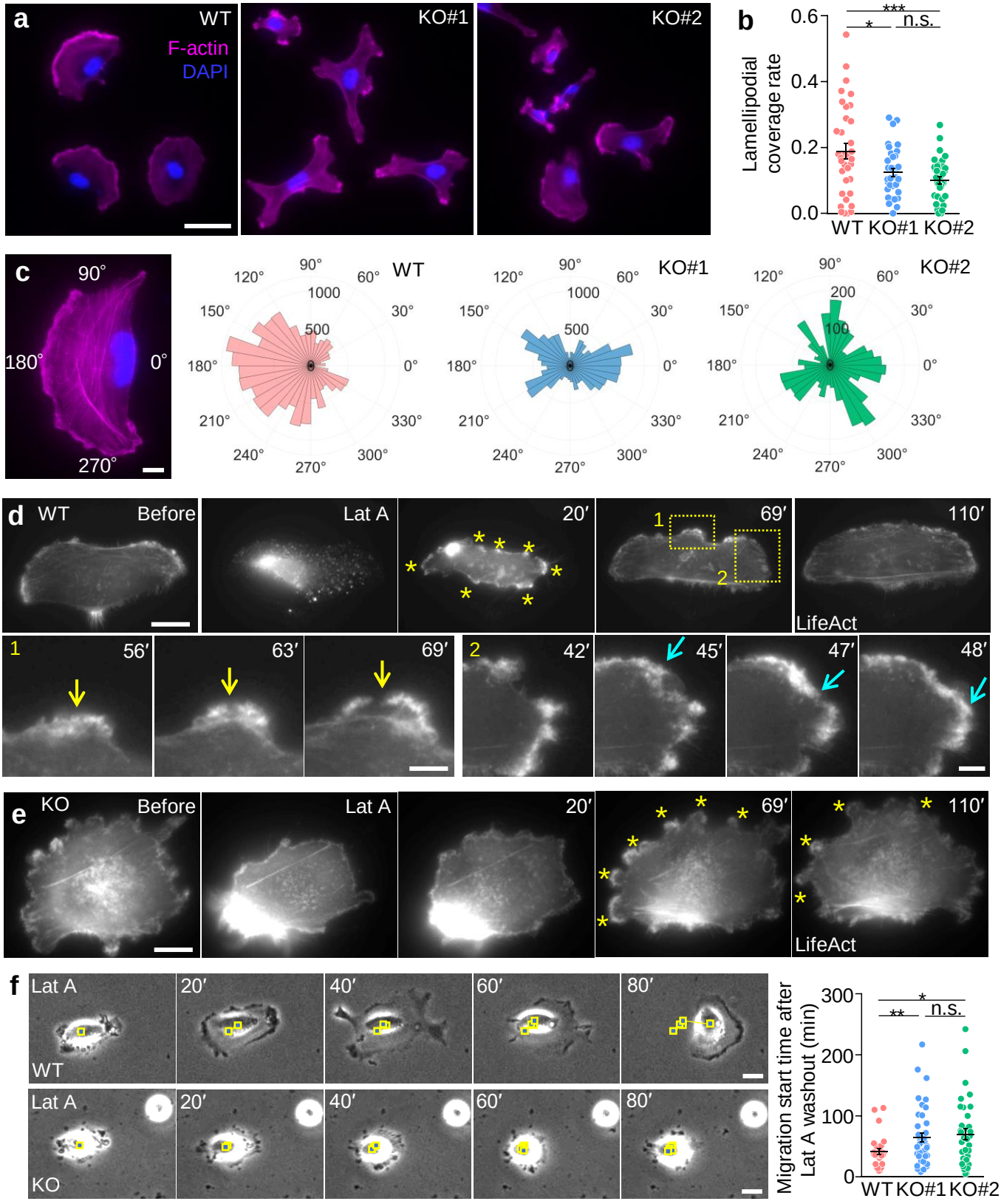

Fig. 5 Yagami et al.

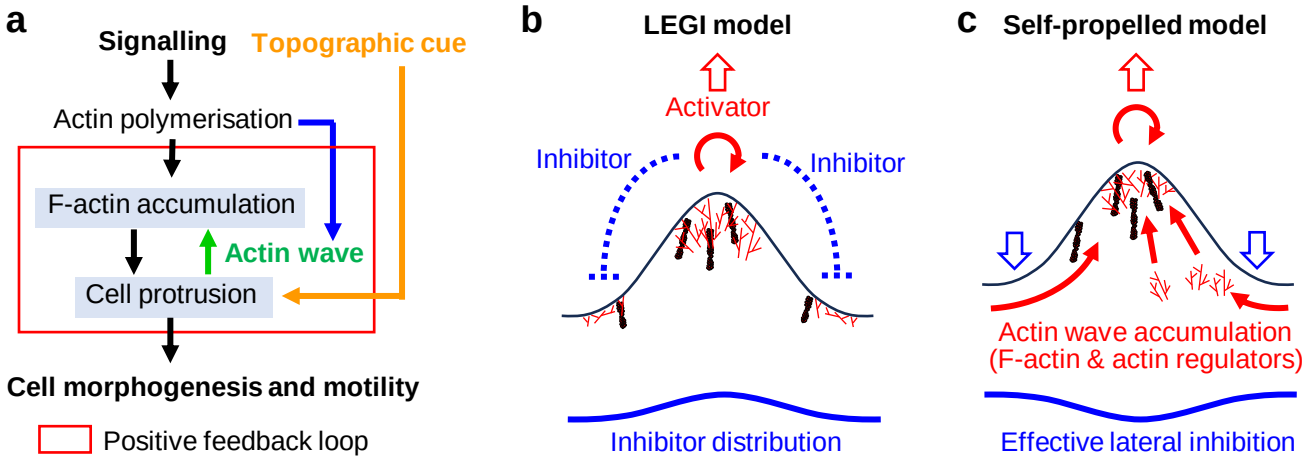

Extended Data Fig. 1 Yagami et al.

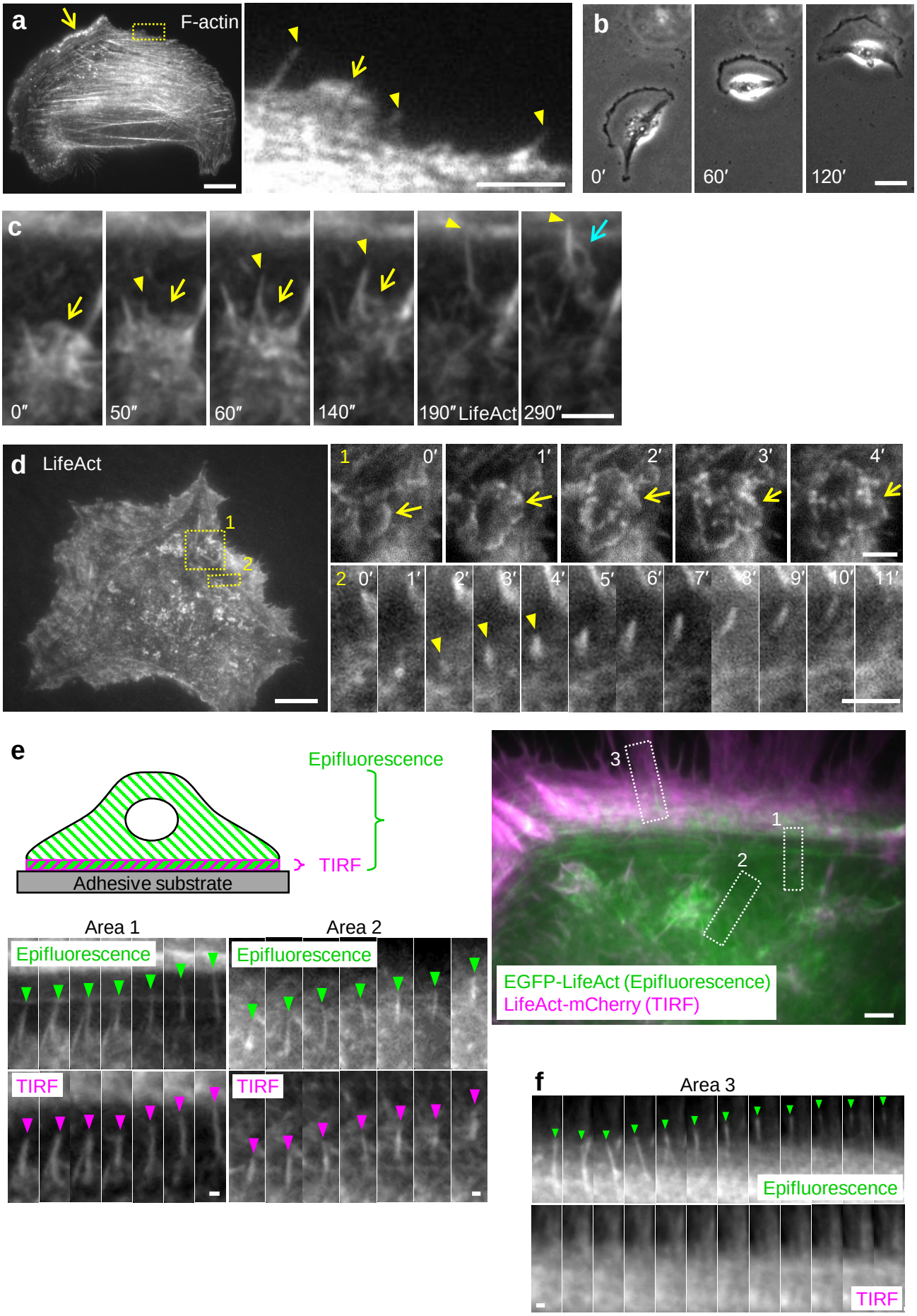

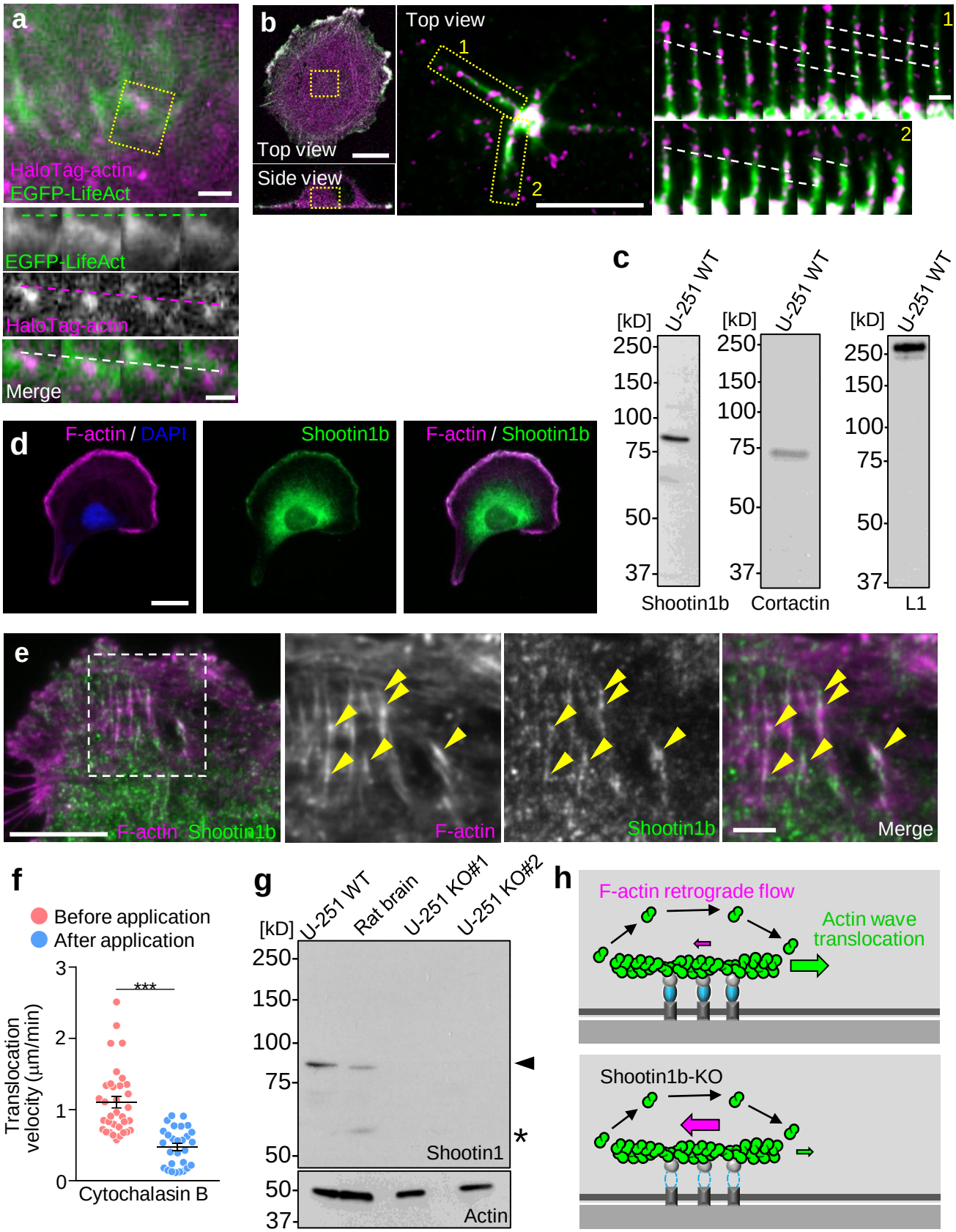
a
HaloTag-actin
EGFP-LifeAct
EGFP-LifeAct
HaloTag-actin
Merge
b
Top view
Side view
Top view
1
2
1
2
c
U-251 WT
[kD]
250
150
100
75
50
37
Shootin1b
Cortactin
L1
d
F-actin / DAPI
Shootin1b
F-actin / Shootin1b
e
F-actin Shootin1b
F-actin
Shootin1b
Merge
f
Before application
After application
Translocation velocity (μm/min)
3
2
1
0
***
Cytochalasin B
g
U-251 WT
Rat brain
U-251 KO#1
U-251 KO#2
[kD]
250
150
100
75
50
Shootin1
*
50
37
Actin
h
F-actin retrograde flow
Actin wave translocation
Shootin1b-KO

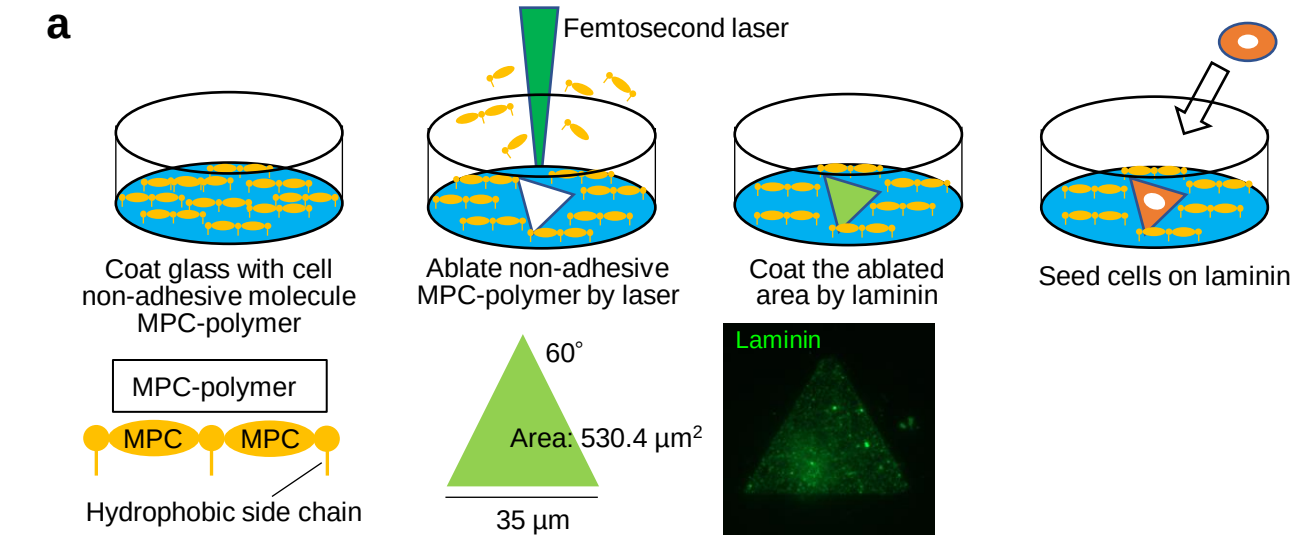
a
Femtosecond laser
Coat glass with cell non-adhesive molecule MPC-polymer
Ablate non-adhesive MPC-polymer by laser
Coat the ablated area by laminin
Seed cells on laminin
MPC-polymer
MPC
MPC
Hydrophobic side chain
60°
Area: 530.4 μm²
35 μm
Laminin

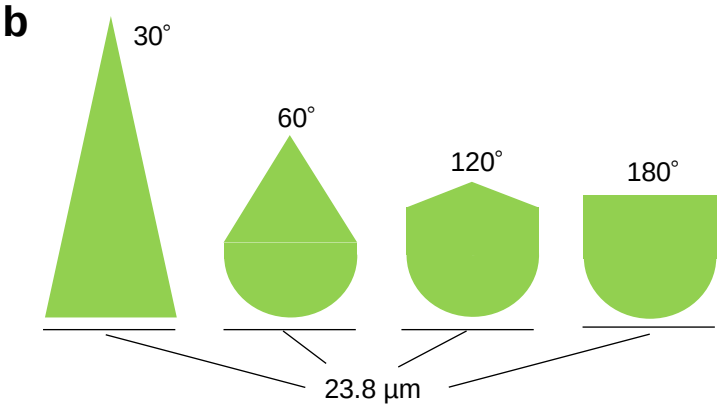
b
30°
60°
120°
180°
23.8 μm

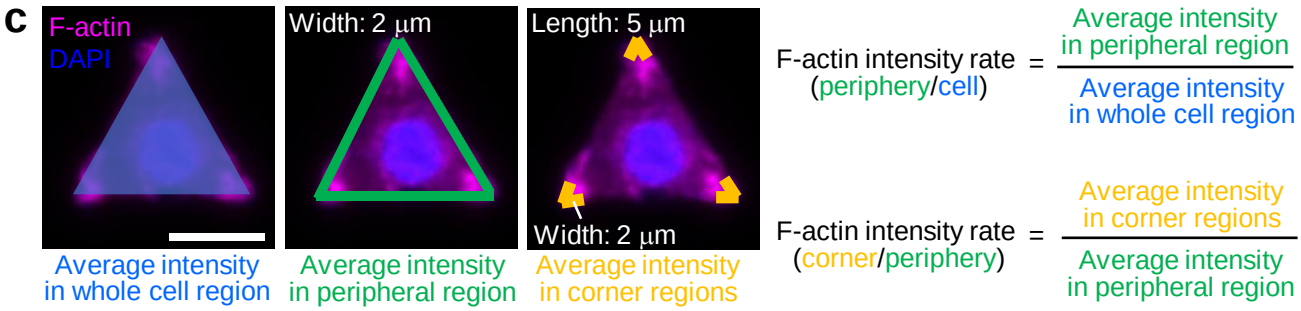
c
F-actin
DAPI
Width: 2 μm
Length: 5 μm
Width: 2 μm
Average intensity in whole cell region
Average intensity in peripheral region
Average intensity in corner regions
F-actin intensity rate (periphery/cell) = Average intensity in peripheral region / Average intensity in whole cell region
F-actin intensity rate (corner/periphery) = Average intensity in corner regions / Average intensity in peripheral region

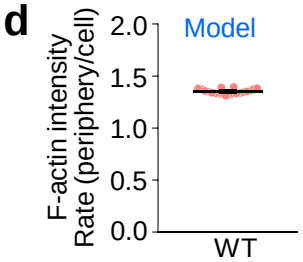
d
Model
F-actin intensity Rate (periphery/cell)
2.0
1.5
1.0
0.5
0.0
WT

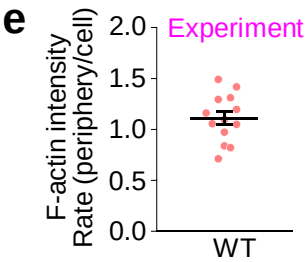
e
Experiment
F-actin intensity Rate (periphery/cell)
2.0
1.5
1.0
0.5
0.0
WT

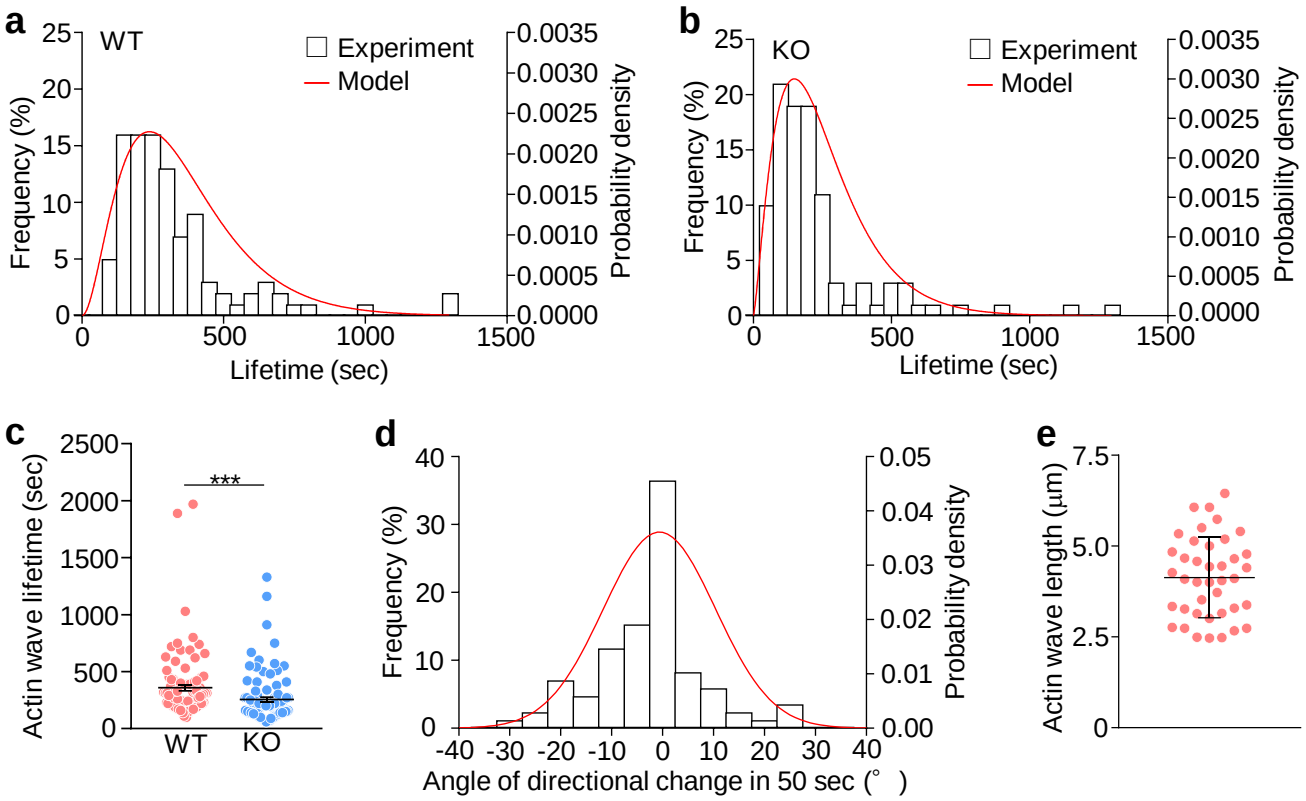
a
WT
Experiment
Model
Frequency (%)
Probability density
Lifetime (sec)
b
KO
Experiment
Model
Frequency (%)
Probability density
Lifetime (sec)
c
Actin wave lifetime (sec)
***
WT
KO
d
Frequency (%)
Probability density
Angle of directional change in 50 sec (°)
e
Actin wave length (μm)

a

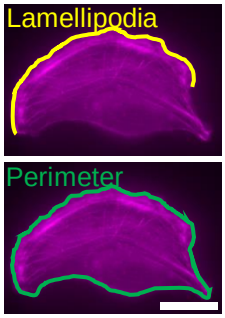

$$\text{Lamellipodial coverage rate} = \frac{\text{Length of lamellipodia}}{\text{Perimeter of cell}}$$

b

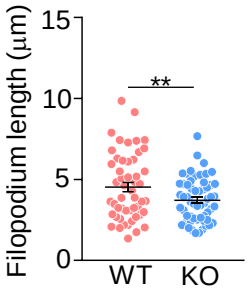
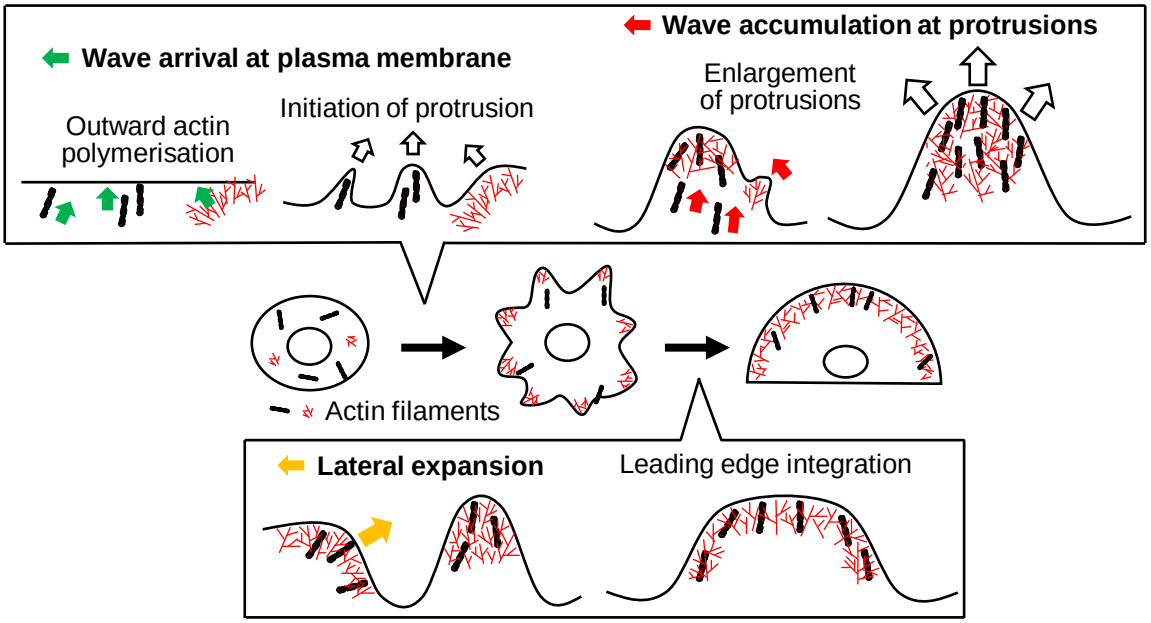
Extended Data Fig. 6 Yagami et al.